From Physics Analysis to Detector Upgrades:

Search for anomalous gauge couplings and upgrades to the ATLAS Liquid Argon calorimeter

Laura Gonzalez Escudero

Supervisor: Prof. Brigitte Vachon

Department of Physics

McGill University

Montreal, Quebec, Canada

August 13, 2025

A thesis submitted to McGill University in partial fulfillment of the requirements of the degree of Master of Science

Abstract

This thesis presents two complementary contributions to the ATLAS experiment at the CERN Large Hadron Collider. The first is a physics analysis of the rare $pp \rightarrow W\gamma\gamma$ reaction, aimed at probing anomalous quartic gauge couplings within an Effective Field Theory framework. Limits are set on dimension-8 operators, with the strongest sensitivity to T-type operators ($\mathcal{O}_{T,5}$ and $\mathcal{O}_{T,6}$), providing new constraints on corresponding Wilson coefficients. The 95 $\%$ confidence intervals were found to be -1.3 TeV$^{-4} < \frac{f_{T,5}}{\Lambda^4} < 1.3$ TeV^{-4} and -1.7 TeV$^{-4} < \frac{f_{T,6}}{\Lambda^4} < 1.6$ TeV^{-4}, demonstrating competitive sensitivity. Additionally, a two-dimensional likelihood scan was also performed to assess parameter correlations, producing constraints consistent with the one-dimensional confidence intervals.

The second contribution supports the Phase-II upgrade of the ATLAS Liquid Argon calorimeter electronics. High-speed optical data transmission using the Core1990 protocol was successfully demonstrated between a Field Programmable Gate Array (FPGA) device emulating the functionalities of the future digital signal processing system, and a prototype Global Event Processor (GCMv3) designed for the future trigger system. Data transfer tests achieved up to 90 $\%$ bandwidth utilization, a latency of 300 ns, and zero bit errors over extended testing. All measurements are in good agreement with theoretical expectations and exceed the new requirements of the Trigger and Data AcQuisition systems.

Together, these efforts enhance both the discovery potential for new physics and the technical readiness of ATLAS for the High-Luminosity LHC era.

Abrégé

Cette thèse présente deux contributions complémentaires à l'expérience ATLAS du Grand Collisionneur de Hadrons (LHC) du CERN. La première est une analyse physique du processus rare $pp \rightarrow W\gamma\gamma$, visant à sonder les couplages de jauge quartiques anormaux dans le cadre d'une théorie effective des champs. Des limites sont imposées sur les opérateurs de dimension-8, avec une sensibilité maximale pour les opérateurs de type T ($\mathcal{O}_{T,5}$ et $\mathcal{O}_{T,6}$), ce qui permet de contraindre les coefficients de Wilson correspondants. Les intervalles de confiance à 95 $\%$ ont été déterminés à -1.3 TeV$^{-4} < \frac{f_{T,5}}{\Lambda^4} < 1.3$ TeV^{-4} and -1.7 TeV$^{-4} < \frac{f_{T,6}}{\Lambda^4} < 1.6$ TeV^{-4}, démontrant une sensibilité compétitive. De plus, une analyse bidimensionnelle a permis d'évaluer les corrélations entre paramètres, donnant des contraintes comparables aux intervalles de confiance unidimensionnels.

La deuxième contribution appuie la mise à niveau de Phase-II de l'électronique du calorimètre à argon liquide d'ATLAS. La transmission optique de données à haute vitesse, utilisant le protocole Core1990, a été démontrée avec succès entre un dispositif Field Programmable Gate Array (FPGA) ou un circuit intégré prédiffusé programmable simulant les fonctionnalités du système de traitement numérique du signal, et un prototype de processeur d'événements global (GCMv3) conçu pour le futur système de déclenchement. Les tests de transfert de données ont atteint jusqu'à 90 $\%$ d'utilisation de la bande passante, une latence de 300 ns et aucune erreur de transmission lors de tests prolongés. Toutes les mesures sont en accord avec les attentes théoriques et surpassent les nouvelles exigences des systèmes de déclenchement et d'acquisition de données.

Ensemble, ces travaux renforcent à la fois le potentiel de découverte de nouvelles physiques et la préparation technologique d'ATLAS en vue de l'ère du LHC à haute luminosité.

Acknowledgments

Para papá y mamá,

¿Cómo agradecer a quienes me lo han dado todo? Poco es dedicarles este trabajo. Sin embargo, voy a intentar poner en palabras los frutos de todo su amor y todos sus sacrificios.

A mamá: ¿te acuerdas de todas las tareas que hicimos juntas? Llegó un momento en que ya podía hacerlas sola, pero siempre estuviste ahí: una lonchera lista, despertarme por la mañana, un cafecito para estudiar, conseguir todo lo que necesitaba para las tareas. Mamá, has sido siempre mi mayor apoyo en todo. Yo no habría logrado esto sin ti.

Papá siempre me trajo libros de ciencias, pinturas, cosas para dibujar, e includo hizo mis proyectos. Sin tantas palabras, me dijiste que crees en mí. A ti te debo el querer salir adelante. Si me voy a MIT, es por ti.

A los dos: todo lo que hago es por ustedes y para ustedes. Son el mejor regalo que Dios me ha dado. No me alcanzará la vida entera para pagarles. Solo tengo mucho amor para poder decirles que son los mejores papás del mundo.

A Sofi: mi mejor amiga, mi consejera y mi compañera para toda la vida. Jamás me he sentido sola porque te tengo a ti. Sin tus risas, chistes y occurrencias, no sé cómo hubiera sido mi infancia. Guardaré siempre en mi corazón todos nuestros juegos, que me hicieron quien soy hoy. Estoy muy orgullosa de ti, Sofi.

I want to thank my supervisor, Prof. Brigitte Vachon, for her patience and dedication. She always took the time to explain everything we worked on. Through her mentorship, I've developed a deep passion for knowledge. I'm truly grateful for her guidance.

To the professors in the ATLAS group, Prof. François Corriveau and Andreas Warburton, and to all my colleagues, Raphael, Xingguo, and Eli: thank you for your support over the past two years. A special thanks goes to Raphael, who was always ready to help, welcomed me so warmly at CERN, and who always showed such kindness to everyone in the group.

Thank you, Dr. Ambler, for all your help with this thesis. Ale, thank you for your company and all your jokes that brought much-needed joy throughout this journey.

I am also grateful to all the friends I made along the way. I am the last one to leave McGill, but I carry all of the memories we shared. A very special thanks to Amalia Karalis. You are the friend I never knew I needed, both at McGill and in life. I am beyond thankful for all your advice and our heartfelt conversations. I am proud to call you my friend, Amy.

To those I met at CERN, especially Michelle and Ruben, thank you for making my stay that much more enjoyable. I never felt alone or far from home thanks to you.

And to those outside of physics who have stood by my side: my CEGEP friends and my church friends. All of you have made my life brighter, happier, and more fulfilling. Without even realizing it, each of you has contributed to this work in your own way.

Author's Contributions

All chapters in this thesis have been written by the author, Gonzalez Escudero, under the supervision of Prof. Vachon.

The ATLAS experiment at CERN is a large international collaboration. Its many members are responsible for the construction, operation, and maintenance of the ATLAS detector, as well as the development and maintenance of the software tools used for measurements like the one discussed in this thesis. The work presented in this thesis relies on the efforts of physicists, engineers, staff, and students who make up the collaboration.

In the following bullet points, a brief summary of the author's contributions is given for each chapter.

- Chapter 1: The author introduces the content of the thesis, and explains that there are two main contributions and how they relate to one another.

- Chapter 2: The author presents a complete overview of the theoretical background necessary for the reader to understand the work presented in the thesis. This includes an introduction to the Standard Model and physics beyond the Standard Model. The author also introduces the Effective Field Theory framework that is employed in a later chapter.

- Chapter 3: The author gives an overview of the experimental infrastructure relevant for this thesis. This includes the CERN accelerator complex, the Large Hadron Collider, and the ATLAS experiment. The author places particular emphasis on the liquid argon calorimeter, which is a key component used for both parts of the thesis. The calorimeter is crucial in recording the data used for the reaction discussed in this thesis. The author has also contributed to the development of readout electronics for the liquid argon calorimeter, also presented in this thesis. Additionally, the author has contributed to the monitoring of the ATLAS Calorimeter in the control room during data-taking.

- Chapter 4: This chapter makes up the core of the first part of this thesis. The author introduces the physics process of interest and motivates its relevance in the context of searches for new physics. The full analysis strategy is described and implemented by the author. The author also presents the results with a detailed interpretation.

- Chapter 5: This chapter makes up the core of the second part of this thesis, where the author presents contributions to the ATLAS Liquid Argon Calorimeter Phase-II electronics upgrade for the High-Luminosity LHC. The author provides an overview of the new readout architecture. The author includes a detailed explanation of the hardware and firmware implementation used for data transfer tests. The author also presents the results. All testing procedures, data analysis, and interpretation of results were carried out by the author in collaboration with the ATLAS LAr electronics upgrade team. Collaborators include G. Chatzianastasiou, M. Helbig, A. Straessner, S. Tang, B. Vachon, and M. Vinicius Silva Oliveira.

- Chapter 6: The author summarizes the results of both components of this thesis and explains how they relate to one another and collectively contribute to the ATLAS detector.

Contents

Chapter 1

Introduction

This thesis presents two distinct but complementary contributions to the ATLAS experiment at the Large Hadron Collider, reflecting both the data analysis and instrumentation aspects of high-energy particle physics research. The first part focuses on the investigation of the physics reaction $pp \to W\gamma\gamma$ and its sensitivity to new physics using an Effective Field Theory (EFT) framework. A likelihood-based approach is employed to explore potential deviations from the Standard Model. The theoretical background for this study is first introduced in Section 2.6. The full study is then presented in detail in Chapter 4. The final state dealt with is characterized by the presence of two photons, whose energy and direction are measured by the ATLAS liquid argon calorimeter. This detail ties together the two components of this thesis.

The second part of this thesis addresses the ongoing upgrades to the ATLAS liquid argon calorimeter electronics, with a focus on the data transfer architecture necessary to support the high bandwidth required at the High-Luminosity LHC. This work involves demonstrating the first data transfer between two test electronic components with an emphasis on data integrity and transmission efficiency. A full report is presented in Chapter 5. Upgrades to the liquid argon calorimeter readout are crucial for improving rare physics searches and studies such as the one presented in the first part of this thesis. Together, these two efforts represent contributions both to the interpretation of physics results and the advancement of detector capabilities within the ATLAS collaboration.

Chapter 2

Theoretical Introduction

The Standard Model (SM) of particle physics is the current theoretical framework that describes the properties of all known elementary particles and the electromagnetic, weak, and strong interactions that govern their interactions [1].

The SM provides a remarkably successful framework both in its agreement with experimental data and through its predictive power, making it an excellent theory for understanding the fundamental constituents of matter and their interactions. This chapter presents a general overview of the theoretical concepts relevant to the motivation and understanding of the $pp \to W\gamma\gamma$ reaction discussed in this thesis, with a particular emphasis on the electroweak sector of the SM and gauge boson interactions.

2.1 Overview of the Standard Model

The SM is described by a Lagrangian density function with 19 free parameters. The latter are constants whose values are not predicted by the theory itself but instead must be determined experimentally. The free parameters include: fermion masses, the Cabibbo-Kobayashi-Maskawa (CKM) matrix mixing angles, gauge couplings, and the Higgs self-coupling. The existence of free parameters reflects the fact that the Standard Model is likely an effective theory, a low-energy limit of a more encompassing theory.

Additionally, the SM is a relativistic quantum field theory based on the principles of gauge invariance and local symmetries [2]. The fields of the SM satisfy the local gauge symmetries of the groups [3, 4]:

$$SU(3)_C \times SU(2)_L \times U(1)_Y \tag{2.1}$$

Each gauge group corresponds to one of the three fundamental forces (excluding gravity):

- $SU(3)_C$ represents the symmetry associated with Quantum Chromodynamics, the theory of the strong interaction. The conserved charge of this group is the colour charge C.
- $SU(2)_L \times U(1)_Y$ represents the symmetries of the electroweak interaction, which unifies the electromagnetic and the weak nuclear forces. The L in $SU(2)_L$ refers to the fact that weak interactions only act on left-handed particles [3]. The conserved charge of the $SU(2)$ group is weak isospin I. The subscript Y represents the conserved hypercharge of the $U(1)$ group.

The third component of weak isospin and hypercharge are related via the electric charge, Q [4]:

$$Q = I_3 + \frac{Y}{2} \tag{2.2}$$

2.2 Elementary Particles

The elementary particles of the SM fall into two main categories: fermions, which make up matter, and bosons, which mediate interactions. A visual representation of all the known elementary particles is shown in Figure 2.1.

Fermions

Fermions are spin-1/2 particles further classified into two categories: quarks and leptons. Each category is further organized into three generations of elementary particles. Particles belonging to different generations differ in their masses. Additionally, for each fermion, there exists a charge conjugate antiparticle [1].

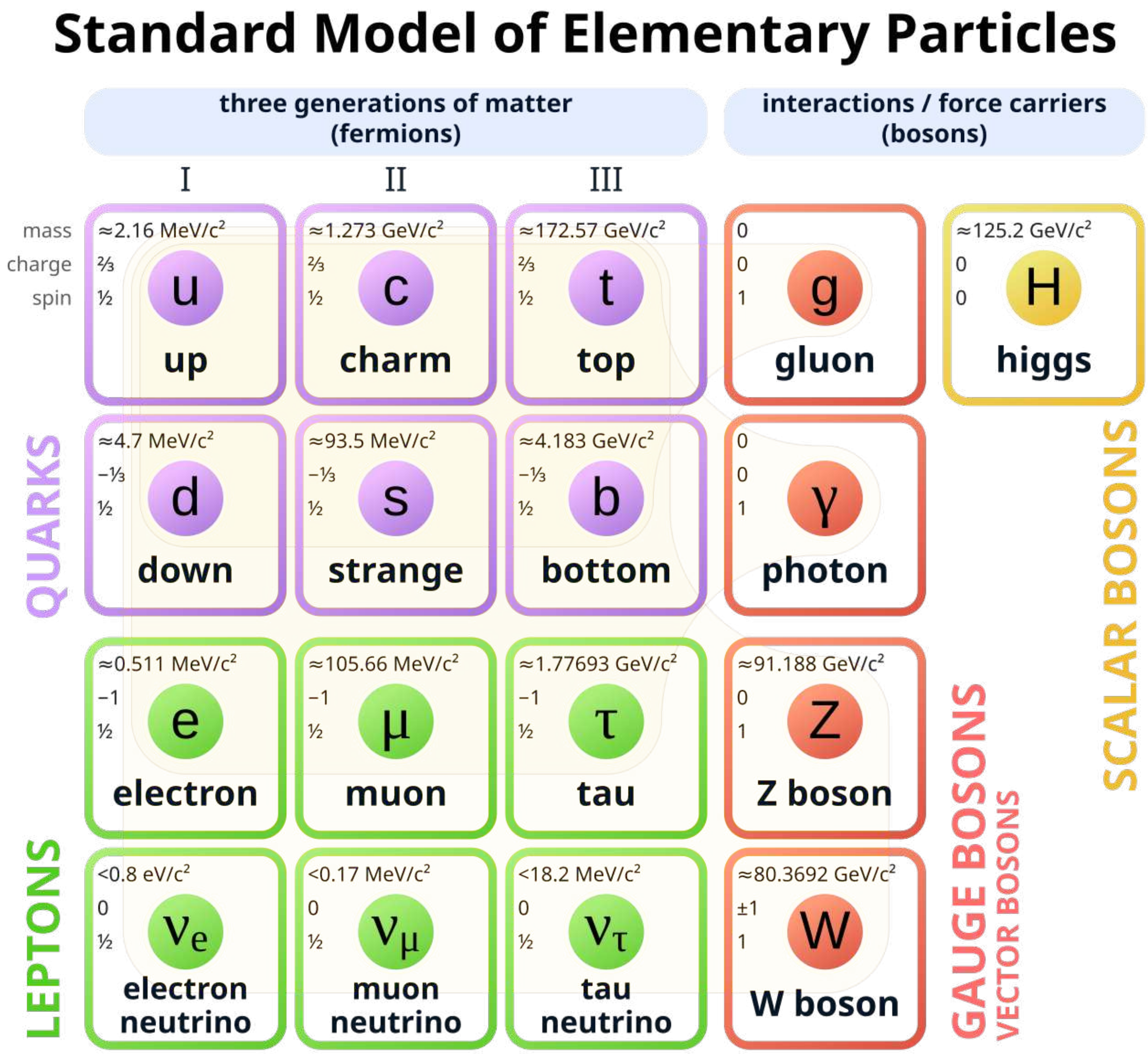

Figure 2.1: Summary of elementary particles making up the Standard Model and their properties: mass, electric charge, and spin. Fermions are grouped into quarks (purple) and leptons (green). Bosons are grouped into gauge bosons (red) and the Higgs boson (yellow) [2].

Quarks are organized into the first, second, and third generation, each with one pair of quarks: (u, d), (c, s), and (t, b), respectively [3]. Quarks participate in all three interactions. As carriers of weak isospin and electric charge, quarks can interact via the electromagnetic and weak forces. Furthermore, as carriers of colour charge (red, green, blue), they can also participate in strong interactions [2]. Due to the properties of the strong force, quarks bind into states called hadrons.

Leptons are organized into three generations depending on the charged lepton flavour accompanied by the corresponding neutrino: (e, ν_e), (μ, ν_μ), and (τ, ν_τ) [3]. Charged leptons interact via the weak and electromagnetic forces; however, neutrinos carry no electric charge and only interact weakly.

Bosons

In the Standard Model, bosons include the mediators of all the fundamental forces and the Higgs boson. The different kinds are categorized depending on their spin. Spin-1 bosons are the force mediators of the electromagnetic, weak, and strong interactions [1]. They are also referred to as *gauge bosons* since they arise from a fundamental symmetry in the SM called gauge invariance [1]. The massless photon γ mediates the electromagnetic interaction between charged particles, and the weak interaction is mediated by massive $W^\pm$ and Z bosons. The strong interaction is mediated by eight massless gluons g [3]. Finally, there is the spin-0 Higgs boson, responsible for giving mass to all elementary particles.

2.3 Gauge Boson Self-Interactions

As the $W^\pm$ bosons are both electrically and weakly charged; in addition to their interaction with leptons and quarks, they can also interact with themselves, with the photon, and with the Z boson, as well as with the leptons and quarks [1].

A central feature of the SM gauge theory is the non-Abelian nature of the $SU(2)_L \times U(1)_Y$ group. A non-Abelian group is one where the group elements do not commute. For example, generators of the group, like T^a, do not commute, satisfying the Lie algebra relation [5]:

$$[T^a, T^b] = if^{abc}T^c \neq 0 \tag{2.3}$$

where the indices a, b, c label the generators over the Lie algebra. This non-commutativity is encoded in the structure constant f^{abc}. This constant affects the field strength tensor $F^a_{\mu\nu}$ that gives rise to the dynamics and interactions between group elements [4]. For a non-Abelian group, the field strength tensor is given by [5]:

$$F^a_{\mu\nu} = \partial_\mu A^a_\nu - \partial_\nu A^a_\mu - gf^{abc}A^b_\mu A^c_\nu \tag{2.4}$$

where A_μ is the gauge field defined as $A_\mu = A^a_\mu T^a$ with the generators T^a of the Lie algebra. Constant g is the gauge coupling constant. The third term only appears if the generators do not commute. This term directly leads to self-interactions among gauge bosons. Self-interactions refer to interactions between the gauge bosons themselves, not involving any quarks or leptons. In particular, this leads to triple and quartic gauge couplings (TGCs and QGCs) involving the electroweak bosons. In the SM, the strength of triple and quartic gauge boson couplings is fully determined by the structure of the gauge boson self-interactions [6]. Notably, the rate of the reaction $pp \to W\gamma\gamma$ depends on the strength of a quartic gauge coupling, which is completely specified in the SM.

2.4 Feynman Diagrams

Feynman diagrams are a graphical representation of particle interactions that provide a pictorial and systematic way to calculate the scattering amplitude (or matrix element) $\mathcal{M}$ of an interaction. This scattering amplitude encodes the probability of a possible process allowed by the Standard Model [4] to occur. The scattering amplitude $\mathcal{M}$ itself is determined using the *Feynman Rules* applied to the relevant Feynman diagrams. These rules associate a term for each incoming and outgoing line in a diagram to conserve energy, momentum, and spin, a term for each internal line representing a propagator, and a term for each interaction vertex.

Feynman diagrams represent terms in a perturbative contribution to the scattering amplitude of a given process. Every possible diagram will contribute to the calculation; however, Feynman diagrams with a large number of vertices contribute less to the total amplitude, and can be neglected [4] depending on the coupling constants involved. As such, the value of the scattering amplitude can be approximated by cutting off the calculation at a given order in the perturbative expansion.

The scattering amplitude $\mathcal{M}$ is directly related to the cross-section, which is the measurable probability for an interaction to occur. The differential cross-section of a process is proportional to the square of the scattering amplitude [4]:

$$\frac{d\sigma}{d\Omega} \propto |\mathcal{M}|^2 \tag{2.5}$$

The scattering amplitude $\mathcal{M}$ encodes the quantum probability of a process, and squaring it gives a probability density. Then, integrating over all internal and external momenta gives the total cross-section σ.

2.5 Beyond the Standard Model of Physics

While the SM has proven to be in excellent agreement with experimental data and to have a strong predictive power, it is not considered a complete theory of fundamental particle physics. Strong theoretical indicators and experimental observations remain unexplained and hint at a theory beyond the SM (BSM).

Theoretical incompleteness includes the many free parameters of the SM that have to be experimentally determined to match observations. Perhaps one of the most significant examples of this is neutrino masses, which were originally assumed to be zero [7]. Later, the observation of neutrino oscillations proved that neutrinos have small but non-zero masses [8]. Additionally, the matter described by the Standard Model makes up about 5 % of the energy content of the universe. Astrophysical and cosmological observations, including galaxy rotation curves, gravitational lensing, and cosmic microwave background measurements, strongly suggest the existence of non-luminous, non-baryonic matter, called dark matter, that interacts gravitationally. Although the SM contains no viable dark matter candidate, it is hypothesized to exist and make up approximately 25 $\%$ of the energy content of the universe. The remaining 70 $\%$ is believed to be made up of dark energy, responsible for the accelerating expansion of the universe [2].

The push for physics beyond the Standard Model also arises from theoretical shortcomings that point to deeper principles that cannot be explained with the framework originally proposed. It is well known that gravity, one of the fundamental forces of nature, and Einstein's general relativity description of gravity, have yet to be reconciled with quantum mechanics, and thus cannot be described by the Standard Model [3]. Furthermore, the original SM does not explain the mass mechanism through which neutrinos acquire mass. The Higgs mechanism alone cannot explain the small neutrino masses. Instead, accommodating neutrino masses requires the addition of right-handed neutrinos to the SM, new mass mechanisms like the see-saw model, and reconsidering the nature of some fundamental particles like the Majorana or Dirac nature of neutrinos [2]. The Standard Model also does not have a mechanism to explain the observed matter/anti-matter asymmetry of the universe. Even if Quantum Chromodynamics allows for a Charge Conjugation Parity violating term of the CKM matrix, experimental limits suggest this term is vanishingly small, requiring fine-tuning of the theory parameters [9].

These experimental and theoretical issues collectively highlight the need to extend the SM to include new physics. The search for phenomena beyond the SM includes efforts like introducing new particles, modifying symmetries, or embedding the theory within a more comprehensive framework. A key strategy in the search for BSM physics lies in testing the predictions of the SM at high precision. The next chapter highlights a theoretical technique used to parameterize possible new physical phenomena in a model-independent approach.

	WWWW	WWZZ	WWγZ	WW$\gamma\gamma$	ZZZZ	ZZZγ	ZZ$\gamma\gamma$	Z$\gamma\gamma\gamma$	$\gamma\gamma\gamma\gamma$
$\mathcal{O}_{S,0}$, $\mathcal{O}_{S,1}$	✓	✓			✓				
$\mathcal{O}_{M,0}$, $\mathcal{O}_{M,1}$, $\mathcal{O}_{M,6}$, $\mathcal{O}_{M,7}$	✓	✓	✓	✓	✓	✓	✓		
$\mathcal{O}_{M,2}$, $\mathcal{O}_{M,3}$, $\mathcal{O}_{M,4}$, $\mathcal{O}_{M,5}$		✓	✓	✓	✓	✓	✓		
$\mathcal{O}_{T,0}$, $\mathcal{O}_{T,1}$, $\mathcal{O}_{T,2}$	✓	✓	✓	✓	✓	✓	✓	✓	
$\mathcal{O}_{T,5}$, $\mathcal{O}_{T,6}$, $\mathcal{O}_{T,7}$		✓	✓	✓	✓	✓	✓	✓	✓
$\mathcal{O}_{T,8}$, $\mathcal{O}_{T,9}$					✓	✓	✓	✓	✓

Table 2.1: All aQGC dimension-8 operators with the gauge boson self-interaction vertices they contribute to. The form of each operator is described in [10, 11].

2.6 Effective Field Theory

In the search for physics beyond the Standard Model, it is often the case that the energy scale of new physics is assumed to lie beyond the direct reach of current experiments, as it would otherwise have been observed already [3]. Nevertheless, the indirect effects of new physics may still be observable at lower, accessible energies. Effective Field Theory (EFT) provides a systematic framework for parameterizing these effects in a model-independent way by extending the Standard Model Lagrangian ($\mathcal{L}_{SM}$) with higher-dimension operators suppressed by powers of a large new physics energy scale, Λ. The additional terms go beyond the set of renormalizable operators of dimension $n = 4$ already present in the Standard Model Lagrangian. This theoretical framework allows the description of the dynamics of a system at a certain energy scale without necessarily requiring a detailed understanding of the underlying interactions at higher energies. The EFT extended Standard Model Lagrangian is shown below [10, 11]:

$$\mathcal{L}_{SMEFT} = \mathcal{L}_{SM} + \sum_{n=5}^{\infty} \frac{f_n}{\Lambda^{n-4}} \mathcal{O}_n \tag{2.6}$$

Equation 2.6 is known as the Standard Model Effective Field Theory (SMEFT) Lagrangian ($\mathcal{L}_{SMEFT}$), where f_n represents dimensionless coupling coefficients, $\mathcal{O}_n$ are n-dimension operators with $n > 4$, and Λ is a characteristic energy scale of physics beyond the SM.

2.6.1 The Operators

The building blocks of an Effective Field Theory are the operators. The operators must preserve the gauge invariance that the SM Lagrangian exhibits. Thus, for an arbitrary gauge transformation U, the following symmetries must be respected:

$$\begin{aligned} \phi' &\to U\phi \\ D'_\mu \phi' &\to U D_\mu \phi \\ \hat{W'_{\mu\nu}} = \sum_j W^j_{\mu\nu} \frac{\sigma^j}{2} &\to U \hat{W_{\mu\nu}} U^\dagger \\ B'_{\mu\nu} &\to B_{\mu\nu} \end{aligned} \tag{2.7}$$

where $D_\mu = (\partial_\mu + igW^j_\mu \frac{\sigma^j}{2} + \frac{i}{2} g' B_\mu)$ is the covariant derivative, ϕ is the Higgs field, σ^j are the Pauli matrices, W_μ and B_μ are the $SU(2) \times U(1)$ gauge bosons, and $W^i_{\mu\nu}$, $B_{\mu\nu}$, g, and g' are their corresponding field strength tensors and gauge coupling constants [11].

Writing down all operators consistent with these symmetries up to dimension-4 gives back the Standard Model Lagrangian. Continuing to higher dimensions gives rise to anomalous couplings. The definition of operators is discussed in more detail in [11].

2.7 Anomalous Quartic Gauge Couplings

Any deviation from the SM-predicted form of quartic gauge couplings is referred to as an anomalous coupling and provides a sensitive probe for BSM physics. The study of physics reactions predicted to exist in the SM that directly proceed through quartic gauge couplings can be used to set constraints on coupling coefficients of higher-dimensional operators that can encode new physics effects.

Anomalous quartic gauge couplings (aQGC) can be systematically described in the SMEFT framework by introducing dimension $n > 4$ operators to Equation 2.6. These operators involve combinations of electroweak field strengths and Higgs doublets. The lowest dimension operators that generate aQGC without simultaneously affecting TGCs first appear at dimension-8 [11]. Different types of dimension-8 operators contribute to genuine quartic vertices. They can be classified into three groups:

- **S-type:** Terms that contain four covariant derivatives of the Higgs field;
- **M-type:** Terms exhibiting two Higgs covariant derivatives and two field strength tensors;
- **T-type:** Terms presenting four field strength tensors.

A summary of all dimension-8 operators contributing to different aQGC vertices is shown in Table 2.1. The operators that give rise to the $W\gamma\gamma$ final state relevant to this work are highlighted in grey. These include M and T-type operators. A complete definition of these operators can be found in [10, 11].

Chapter 3

Experimental Setup

In this chapter, a brief overview of both the Large Hadron Collider (LHC) and the ATLAS detector, with a focus on the liquid calorimeter system relevant for the work in this thesis, is presented. On one hand, the $pp \to W\gamma\gamma$ reaction relies on the detection of photons, which is done at the calorimeter level. On the other hand, all upgrade efforts presented in this thesis are intended for the liquid argon calorimeter upgrade.

3.1 The Large Hadron Collider

The Large Hadron Collider is the world's most powerful particle accelerator and is located in the CERN accelerator complex, shown in Figure 3.1, which straddles the border between Switzerland and France. The LHC is installed in a 26.7 km long circular tunnel 100 m below the surface [12]. It consists of two parallel beam lines held at ultrahigh vacuum through which two counter-rotating proton or ion beams travel near the speed of light.

The LHC provides the last stage of acceleration after a long chain of accelerators. At the start of the chain, protons are stripped from hydrogen atoms using electric fields. The protons are accelerated to 50 MeV inside the Linear Accelerator 2, after which they are injected into the Booster, which accelerates them to 1.4 GeV. Following this step, protons are accelerated to 25 GeV in the Proton Synchrotron, and the Super Proton Synchrotron accelerates them further to 450 GeV.

Finally, the LHC accelerates the protons to 6.5 TeV to achieve a final collision center of mass energy of 13 TeV [13].

The LHC uses superconducting radio frequency (RF) cavities for proton acceleration and superconducting dipole and quadrupole magnets for beam handling, such as focusing and bending. In addition to accelerating the protons, the RF cavities are used to keep the protons in bunches and spaced 25 ns apart [12].

The number of proton-proton interactions per bunch crossing is quantified using a quantity called the instantaneous luminosity L. It depends only on the beam parameters; further discussions and calculations are found in [12]. The instantaneous luminosity can also be defined in terms of the total proton-proton cross-section σ_{pp} and the rate of proton-proton interactions dN/dt:

$$L = \frac{1}{\sigma_{pp}} \frac{dN}{dt} \tag{3.1}$$

Furthermore, the integrated luminosity $\mathcal{L}$ provides a measure of the total number of collisions produced over a period of time:

$$\mathcal{L} = \int L dt \tag{3.2}$$

The total integrated luminosity can be used to calculate the number of collisions resulting from a particular physics process with total cross-section σ:

$$N_{events} = \mathcal{L} \times \sigma \tag{3.3}$$

Essentially, Equation 3.3 shows that the total number of desired events N_{events} is a result of the total number of collisions and the probability of an event to occur σ. In collider experiments, the number of recorded events depends on both the luminosity and the detector efficiency. At higher instantaneous and integrated luminosities, the demands on operational efficiency and hardware robustness become especially significant.

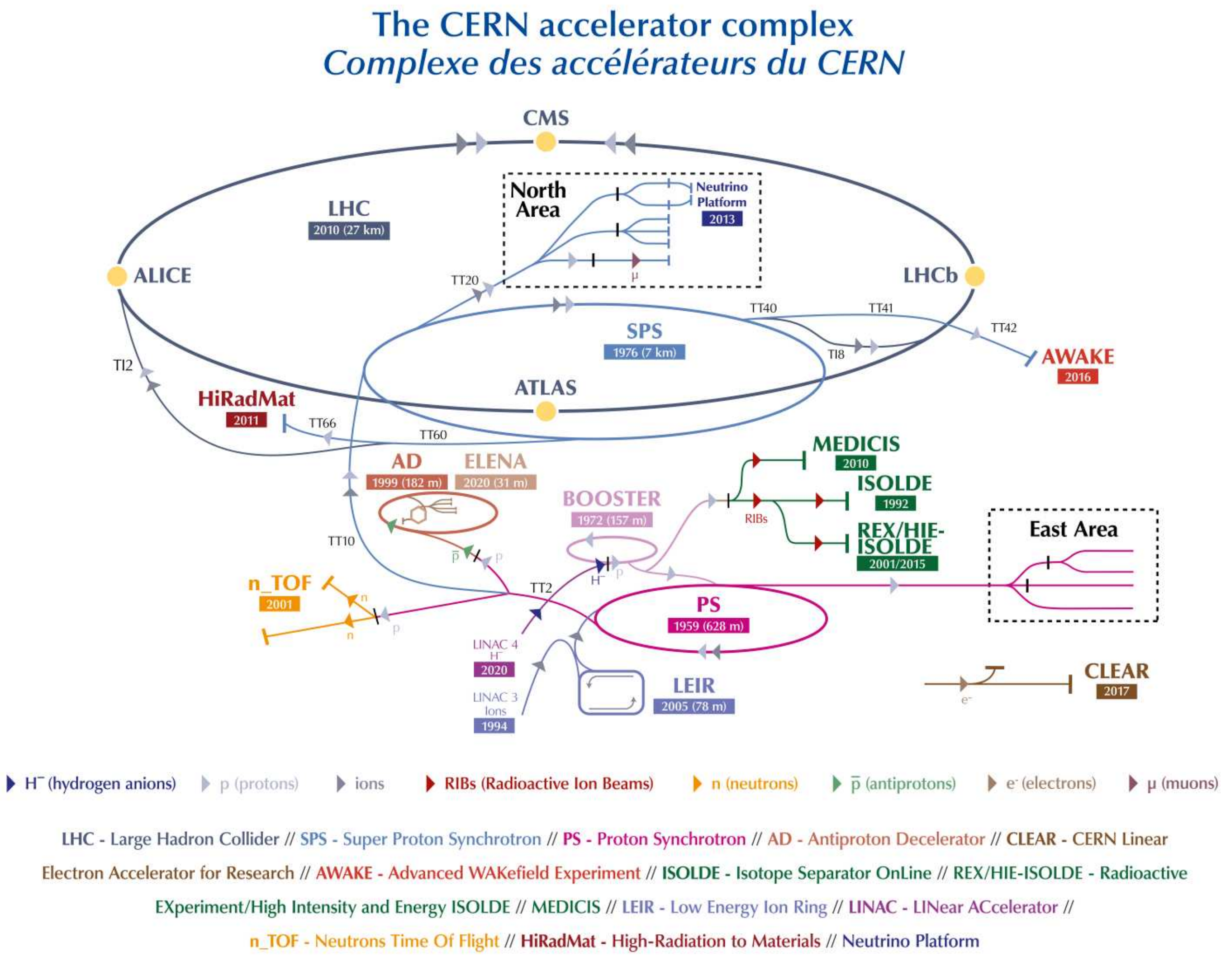

Figure 3.1: Schematic diagram of the CERN accelerator complex [14].

3.2 The ATLAS detector

The ATLAS detector is one of two general-purpose experiments along the LHC ring. It is a cylindrical detector 44 m in length and 25 m in height. A schematic drawing of the ATLAS detector is shown in Figure 3.2. The ATLAS detector was first proposed in 1994 and has been in operation since autumn 2009. It was designed to investigate a broad physics program, including the observation of the Higgs boson, search for new physics, and to make precision measurements of the Standard Model processes and parameters [15].

ATLAS utilizes a multi-layer approach to particle detection, comprising various subsystems around the interaction point. These are designed to identify and reconstruct electrons, photons, muons, and hadronic jets produced in proton-proton collisions. Each sub-detector is optimized to measure the energy and momentum of different particles. All the subsystems are illustrated in Figure 3.2. In increasing radius, the ATLAS sub-detectors are the Inner Detector, the Electromagnetic Calorimeter, the Hadronic Calorimeter, and finally the Muon Spectrometer.

The Inner Detector system provides charged-particle tracking by relying on concentric and complementary systems with different granularities. They each provide a few measurements along a charged particle trajectory. Additionally, the Inner Detector operates in a 2 T solenoidal magnetic field, enabling the identification and momentum measurement of charged particles from the bending of their tracks. The calorimeter system provides energy measurements for electrons, photons, and hadrons. Finally, the Muon Spectrometer comprises high-precision tracking and measures the deflection of muons in a magnetic field to measure their momenta [16].

3.2.1 Calorimeters

The ATLAS calorimeter system is composed of the electromagnetic (EM) calorimeter and the hadronic calorimeter. They are both designed to absorb most of the particles coming from a collision, forcing them to stop and deposit all of their energy within the calorimeter system [16].

Both types of ATLAS calorimeters employ sampling calorimetry with alternating layers of

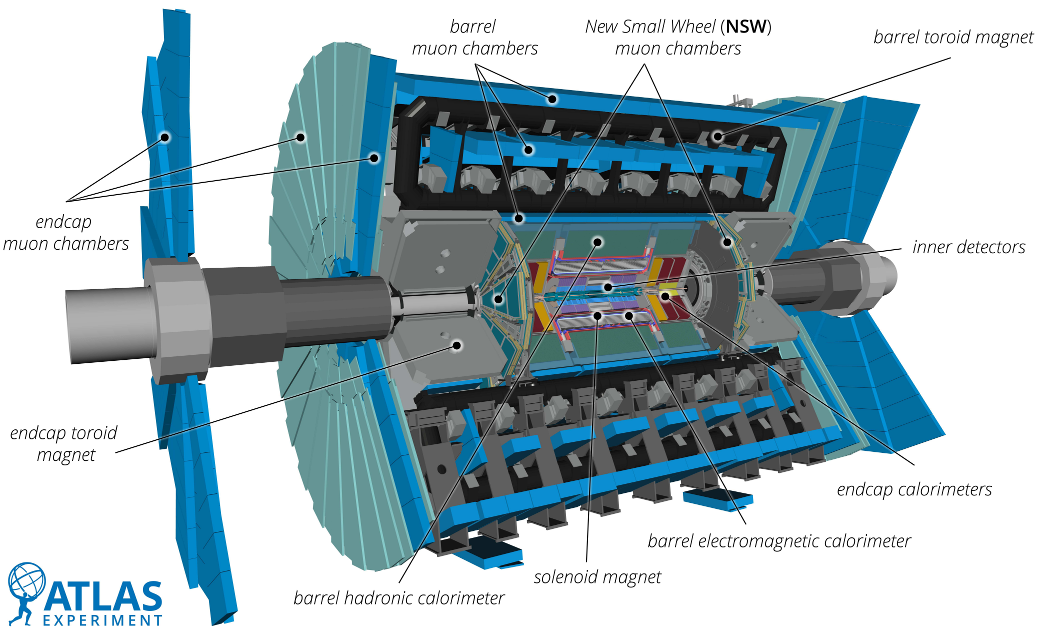

Figure 3.2: Schematic drawing of the ATLAS detector with each detector sub-system indicated. ATLAS has the dimensions of a cylinder, 44 m long and 25 m in diameter [17].

absorber material and active detection material. A sampling calorimeter uses a dense absorber material to induce a particle shower, during which the incoming high-energy particle interacts with the detector material and produces a cascade of secondary particles. The shower energy is then measured as a function of energy deposits along the shower.

At LHC energies, electrons and photons first interact with matter in the calorimeter through bremsstrahlung and pair production, respectively [2]. In an electromagnetic shower, an electron radiates a photon, while photons convert into electron-positron pairs, creating a cascade of secondary particles. The ATLAS electromagnetic calorimeter determines particle energy by measuring the amount of ionization produced in liquid argon by particles in the shower.

In contrast, hadrons primarily interact with the detector material via the strong nuclear force, producing complex hadronic showers [2]. The ATLAS hadronic calorimeter primarily uses scintillating tiles as active material, which emit light when traversed by charged particles. This scintillation light is collected and used to measure the energy of a sample of a hadron-initiated shower. Since both parts of this thesis rely on the liquid argon calorimeter detector, the following discussion will focus on this detector.

3.3 Liquid Argon Calorimeter

In ATLAS, the liquid argon sampling calorimeter uses liquid argon as its active medium and primarily lead metal absorbers [18]. A schematic diagram of the liquid argon calorimeter is shown in Figure 3.3. Charged particles shower in the metal absorber layers, and the secondary particles traverse the liquid argon gaps, producing ionization charges. The ionization electrons and positive ions drift across the liquid argon gap under an electric field. The motion of charges induces a current on the readout electrodes. The current signal is in the form of a triangular pulse [19]. The characteristic triangular shape is due to the mobility of electrons in LAr compared to the mobility of positive ions. The fast rise of the pulse comes from the free electrons moving extremely fast in the electric field, while the long tail is created by the positive ions, which take much longer to reach the cathode [2]. The raw pulse is further shaped with amplifiers and filters. The height of the shaped pulse (after the charge amplifiers) is proportional to the amount of energy deposited in the liquid argon gap.

The Liquid Argon (LAr) system consists of several subsystems, namely the LAr Electromagnetic Barrel Calorimeter, the LAr Electromagnetic Endcap Calorimeter, the LAr Hadronic Endcap Calorimeter, and the LAr Forward Calorimeter. Together, they cover the central region and both ends of the detector. The system measures the energy of electrons and photons, and part of the energy of τ leptons and jets. The system also participates in the calculation of missing transverse energy. Additionally, it provides some information to the calorimeter trigger system to select events potentially containing electrons, photons, τ leptons, jets or E_T^{miss} [15].

The barrel and endcap electromagnetic calorimeters are comprised of accordion-shaped copper-kapton electrodes arranged between lead absorber plates and submerged in LAr [20], as shown in Figure 3.4. This arrangement guarantees full azimuthal ϕ coverage and finer detector granularity near the interaction point [18]. The degree of folding decreases radially and comprises three regions of decreasing granularity, as seen in Figure 3.5. The accordion shape is segmented in both ϕ and η. The latter is pseudorapidity, which is a quantity related to the polar angle θ, and defined as $\eta = -\ln\left(\tan\left(\frac{\theta}{2}\right)\right)$.

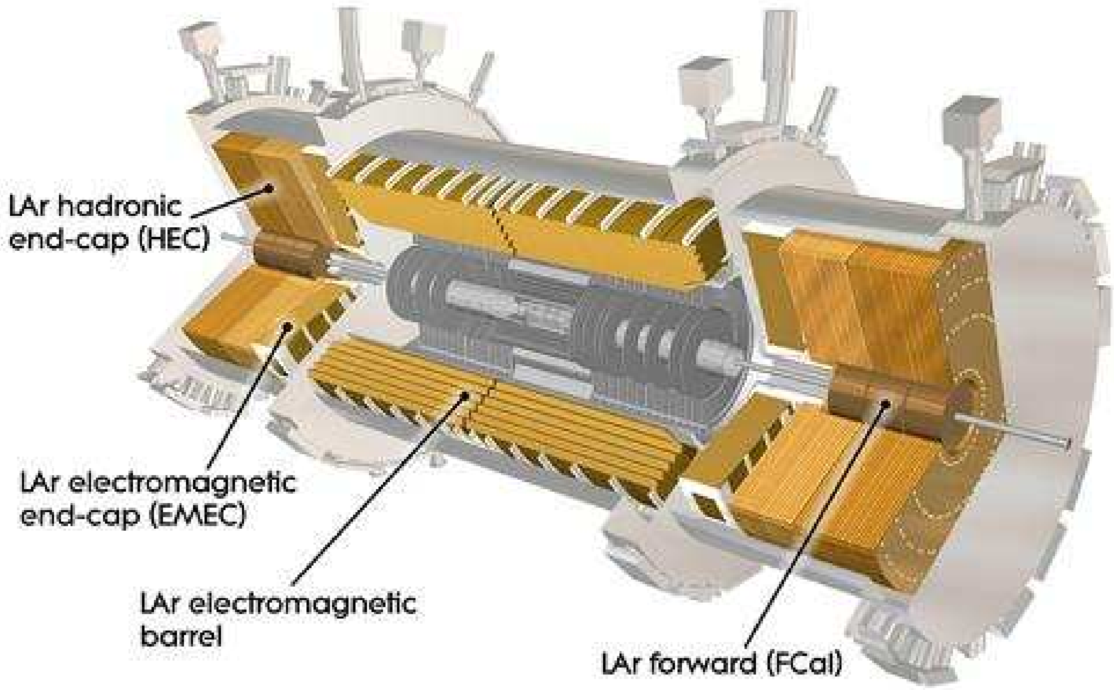

Figure 3.3: Labelled diagram with all components of the ATLAS Liquid Argon Calorimeter. In the barrel, the calorimeter is 6.4 m long, and extends from a radius of $R = 2.8$ m to $R = 4$ m [21].

3.4 Object Reconstruction and Particle Identification in the electromagnetic calorimeter

Particle detection and identification in ATLAS rely on both tracking and calorimetry. Tracking is the reconstruction of the trajectories of charged particles based on the position of energy deposited in the Inner Detector subsystems. Reconstructed trajectories are called tracks. Calorimetry, as

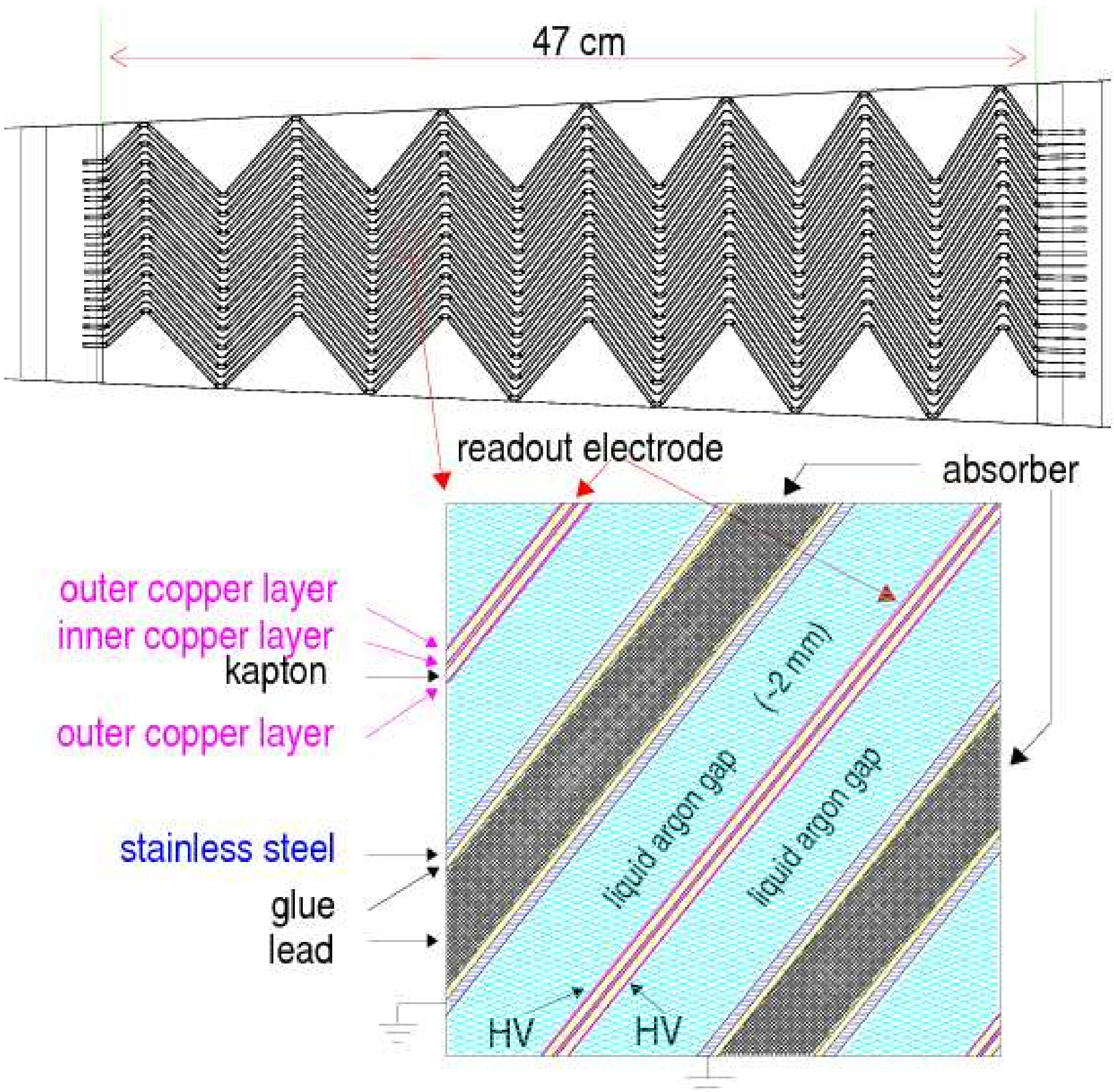

Figure 3.4: Accordion structure of the electromagnetic calorimeter barrel. The top figure is a view of a small segment in the plane transverse to the LHC beams. The bottom figure shows the layering of the liquid argon gap, the lead absorbers, and the copper electrodes [16].

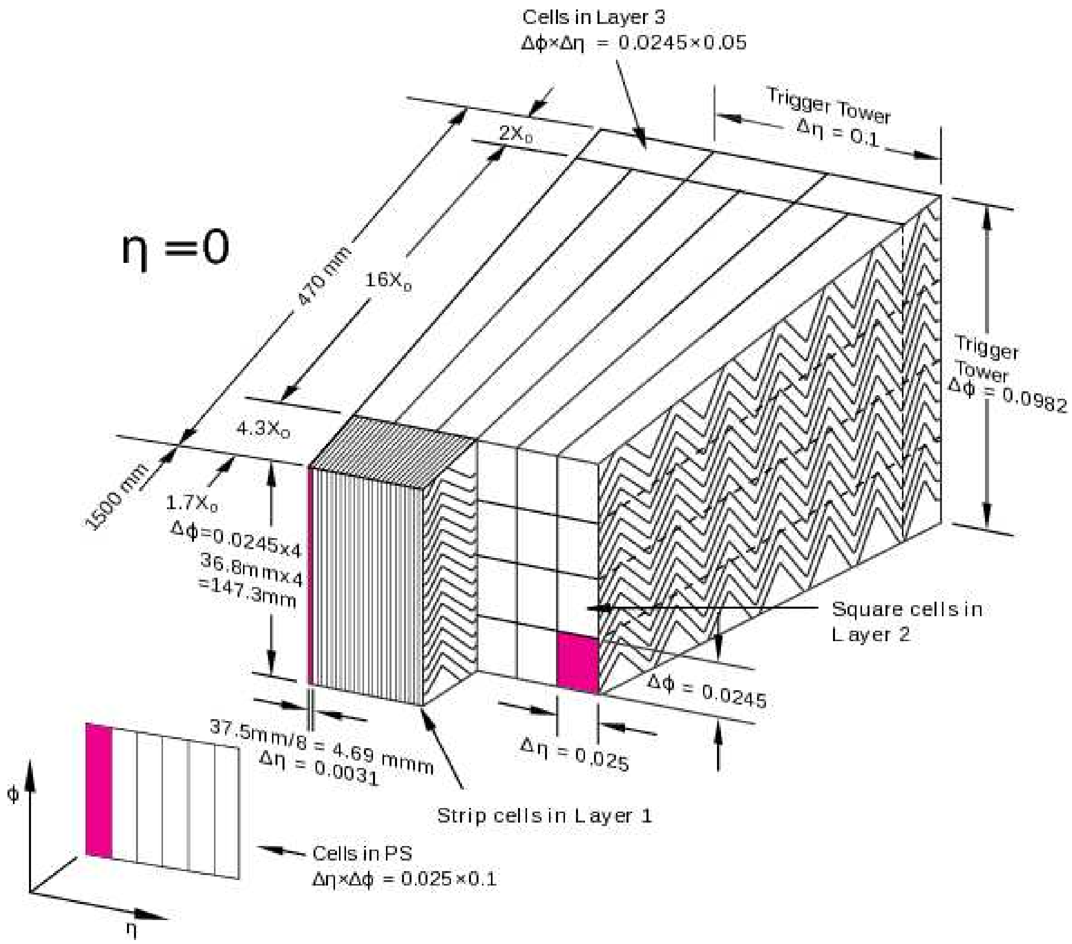

Figure 3.5: Schematic diagram of a segment of the barrel electromagnetic calorimeter showing its geometry and granularity in η and ϕ of all three layers [16].

described before, is the measurement of the energy of a particle. This section briefly describes how the LAr calorimeter is used to detect particles like photons and electrons that are of special interest to the study of the $pp \to W\gamma\gamma$ reaction in this thesis.

The electromagnetic (EM) showers initiated by a photon or electron impinging on the LAr calorimeter are reconstructed using a so-called "sliding-window" algorithm [20]. The algorithm searches for regions of the calorimeter in $\eta \times \phi$ space where a significant amount of energy has been measured within a predetermined window size.

Calorimeter regions where the total energy exceeds a given threshold are identified as cluster seeds [20]. Then, the energy is collected over a predefined area of cells to form a so-called EM cluster [16]. Tracks reconstructed in the inner detector are matched to EM clusters. Different quality criteria are used to classify EM clusters as different particle candidates [20].

Figure 3.6 shows a schematic representation of how each particle of interest interacts with the different ATLAS sub-detectors. The information from all sub-detectors is combined to identify the type of particle based on its unique signature. Of particular interest, photons leave no track in the Inner Detector due to their lack of electric charge but deposit all of their energy in the electromagnetic calorimeter. Electrons, on the other hand, will have a reconstructed track in the Inner Detector and also deposit most of their energy in the electromagnetic calorimeter. Muons rarely initiate showers in the calorimeters and are instead identified by their tracks in the Inner Detector and Muon Spectrometer. Together, this information is used to reconstruct events like the $W\gamma\gamma$ final state of interest in this thesis.

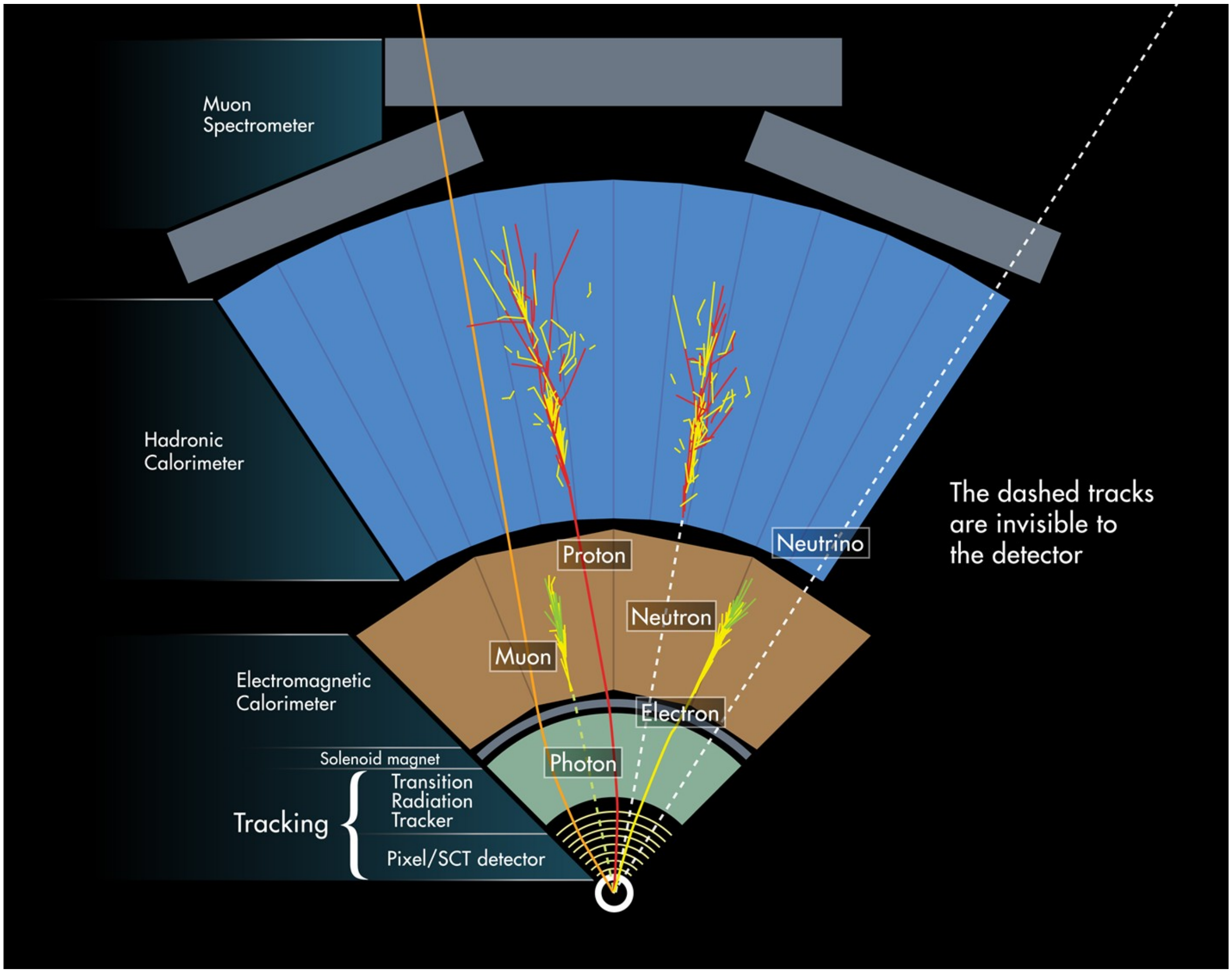

Figure 3.6: Schematic diagram showing how different types of particles interact with each subsystem of the ATLAS detector [22].

Chapter 4

Search for Anomalous Quartic Gauge Couplings

The process $pp \to W\gamma\gamma$, involving the production of a W boson in association with two photons in proton-proton collisions, is an extremely rare but important electroweak process predicted and fully constrained by the Standard Model. The first observation of this process was published in January 2024 by the ATLAS collaboration [23]. The fiducial cross-section of $W(e\nu)\gamma\gamma$ and $W(\mu\nu)\gamma\gamma$ events together was measured to be $\sigma_{fid} = 13.8 \pm 1.1(\text{stat})^{+2.1}_{-2.0}(\text{syst}) \pm 0.1(\text{lumi})$ fb, in agreement with the SM prediction [23].

Although the first observation of the rare $pp \to W\gamma\gamma$ event is consistent with the prediction of the Standard Model, studying this channel remains highly relevant for probing new physics. This process proceeds through a quartic gauge vertex, a key feature that makes it particularly sensitive to deviations from the SM. This chapter focuses on exploring such effects within an Effective Field Theory (EFT) framework by constraining possible couplings associated with higher-dimension operators that parametrize new physics.

4.1 The $pp \to W\gamma\gamma$ Physics Process

The $pp \to W\gamma\gamma$ reaction receives contributions from a set of Feynman diagrams that can be grouped into different topologies and classes of interactions. The main ones are illustrated in Figure 4.1. These include Feynman diagrams in which the photons are produced via $WW\gamma\gamma$ quartic and $WW\gamma$ triple gauge coupling vertices in Figures 4.1(a) and 4.1(b), respectively. Additionally, photons can also be produced via initial or final state radiation, as shown in Figure 4.1(c). In initial-state radiation, one or both photons are emitted by the incoming partons (constituents of protons), while in final-state radiation, one or both photons are emitted by the final-state W boson. Finally, both photons can also be produced through the decay of a Higgs boson [23], as shown in diagram 4.1(d), but with significantly smaller probability. Other contributions, like quark-loops, also contribute to higher order and are often neglected in first approximations as discussed in Section 2.4 and not shown here.

4.2 Motivation

The production of a W boson in association with two photons ($pp \to W\gamma\gamma$) serves as a powerful probe for the Standard Model. The production of three electroweak gauge bosons in proton-proton collisions is extremely rare, with the production of a $W\gamma\gamma$ event being more than 4000 times rarer than the production of a Higgs boson, as shown in Figure 4.2. The fact that the production of $W\gamma\gamma$ is so rare yet observable makes it a powerful test of the Standard Model. The study of this reaction is also important as it will become, with an increasing data set, a background for other electroweak studies.

The $W\gamma\gamma$ final state is a unique laboratory suited to study electroweak gauge structure, anomalous gauge couplings, and directly testing the SM. This process is sensitive to both triple and quartic gauge coupling that could be modified by the presence of new physics phenomena [23]. Any deviations from predictions would directly indicate the existence of new physics. In the absence of any statistically significant deviation from theoretical predictions, studying triboson production can be

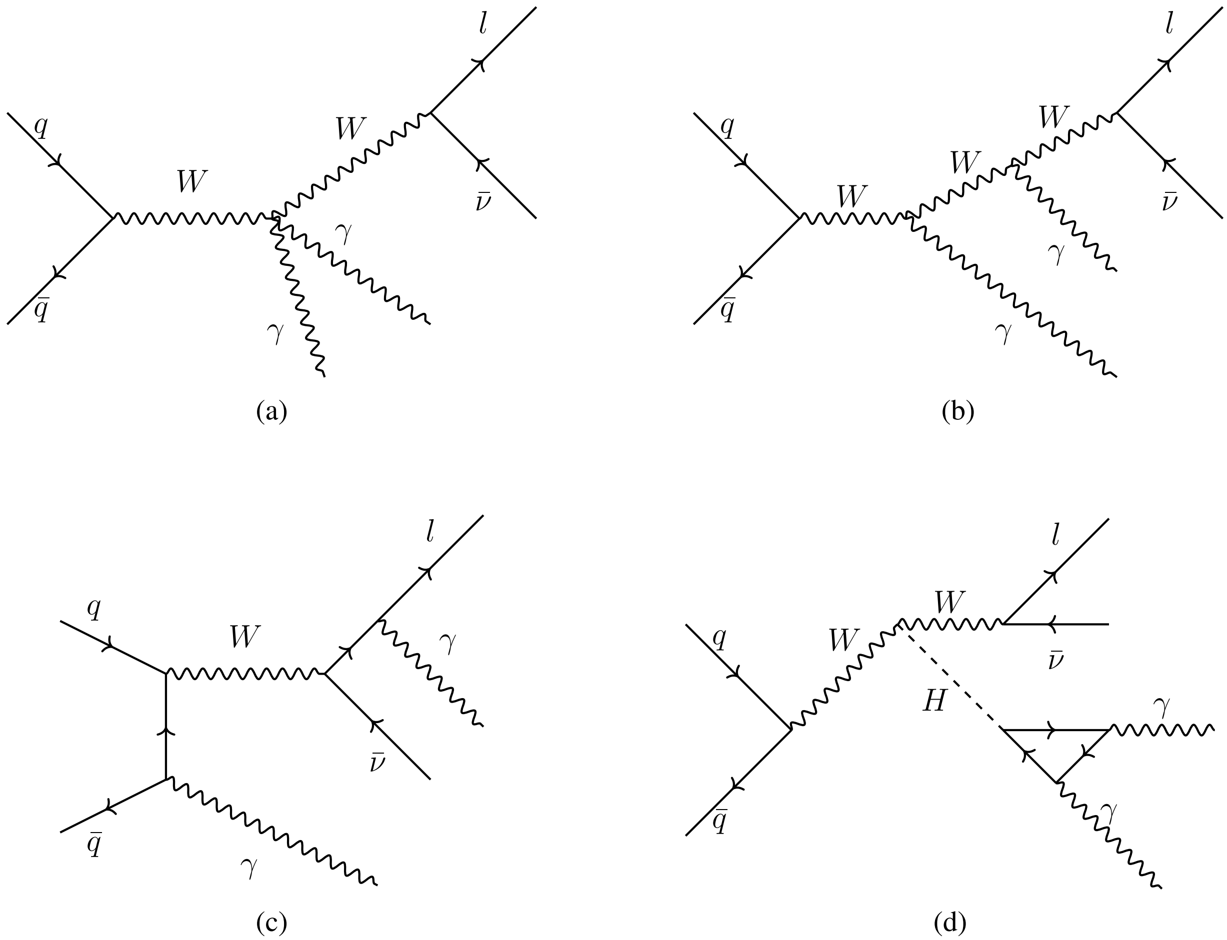

Figure 4.1: Representative Feynman diagrams contributing to the $pp \to W\gamma\gamma \to (l\bar{\nu})\gamma\gamma$ process. Diagrams illustrate different processes in which photons are produced via (a) a $WW\gamma\gamma$ quartic gauge coupling, (b) a $WW\gamma$ triple gauge coupling, (c) both initial and final state radiation, and (d) the decay of a Higgs boson. In all diagrams, the final W boson is shown with its leptonic decay mode into a charged lepton l and its corresponding antineutrino $\bar{\nu}$.

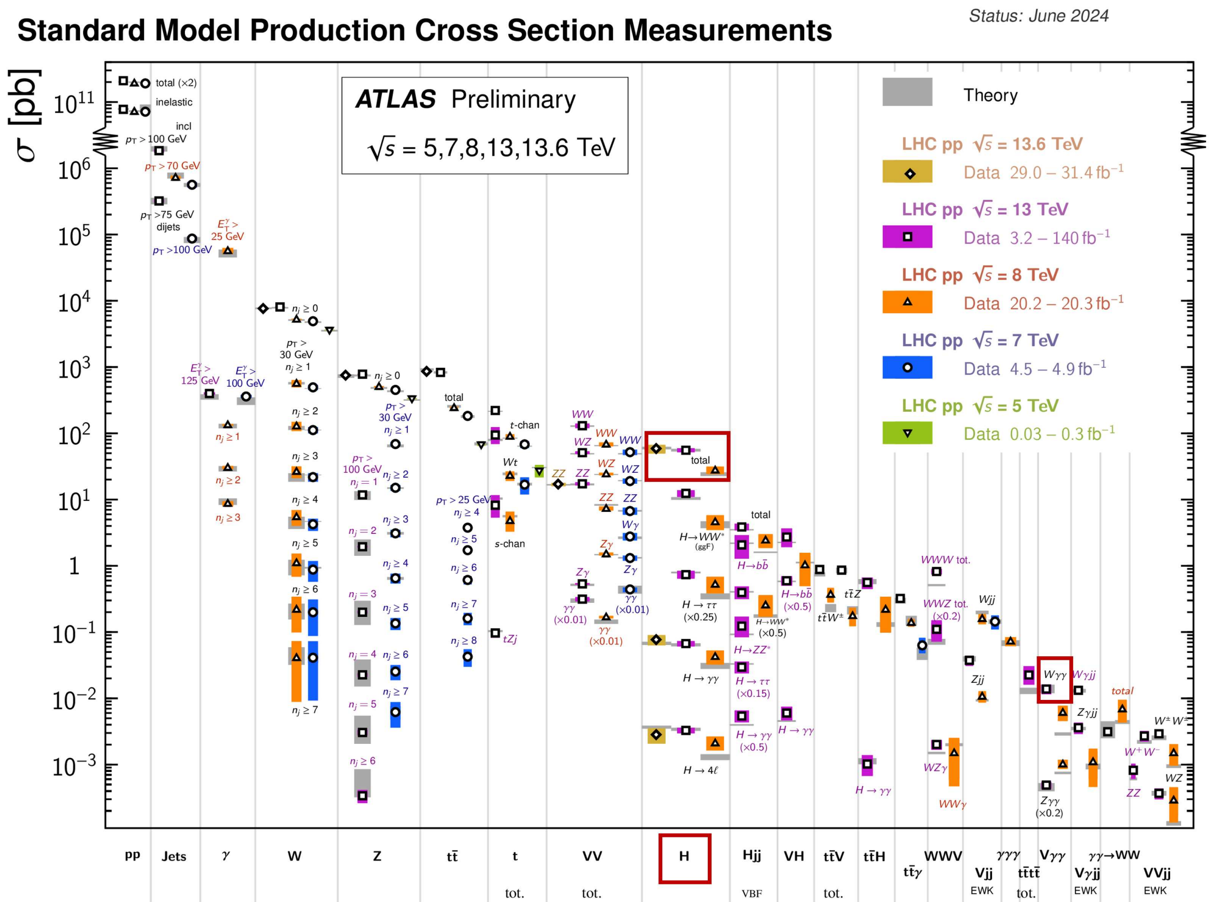

Figure 4.2: Summary of several Standard Model total and fiducial production cross-section measurements. The measurements are shown with corresponding branching fractions and compared to the corresponding theoretical expectations. Final states of interest are highlighted in red for comparison: $W\gamma\gamma$ vs. total Higgs cross-section [24].

used to set constraints on anomalous triple and quartic gauge coupling operators in the context of an Effective Field Theory, described in Section 2.6.

4.3 Overview of the $pp \to W\gamma\gamma$ Cross-section Measurement

This thesis builds upon the analysis presented in [23], which reports the measurement of the inclusive cross-section for the rare Standard Model process $pp \to W\gamma\gamma$ at a center-of-mass energy of $\sqrt{s} = 13$ TeV. This section briefly summarizes the key features of the physics analysis described in the paper and highlights the components that are reused for this thesis.

The present study extends upon this work by performing a differential measurement of the number of events (three bins) of the $W\gamma\gamma$ signal as a function of the transverse momentum of the leading photon, denoted $p_T^{\gamma 1}$. This variable has been identified in earlier effective field theory (EFT) studies as particularly sensitive to potential deviations from the Standard Model induced by dimension-8 operators. Examining the distribution of events across $p_T^{\gamma 1}$ bins, rather than relying on the total number of events, improves the sensitivity to possible anomalous quartic gauge couplings indicative of new physics. The EFT interpretation presented in the following sections is a novel extension of the previously published analysis in [23].

4.4 The $W\gamma\gamma$ Signal and Control Regions

The original analysis defines a Signal Region (SR) characterized by events with a single charged lepton (electron or muon), significant missing transverse energy signalling the presence of a neutrino, and two isolated photons. To estimate and constrain backgrounds, a Control Region (CR) is constructed. The analysis reported an inclusive fiducial cross-section based on the total number of observed events in the SR, with systematic uncertainties driven by photon reconstruction, background models, and theoretical inputs.

The regions described here are discussed in further detail in [23]. Events are categorized into distinct signal and control regions to enhance the sensitivity of the analysis and estimate backgrounds. The signal region is defined by a set of selection criteria optimized to isolate the target final state, where potential EFT effects may manifest. In contrast, control regions are constructed to be enriched in background processes; for this analysis, the top control region is defined to normalize all top background events originating from the production of top quarks. The signal region requires the reconstruction of one charged lepton and two photons in the event. The final states of interest in the $pp \rightarrow W\gamma\gamma$ process are those resulting from the electron and muon decay channels of the W boson. The selection criteria for the signal region SR are summarized in Table 4.1. The

Signal Region
= 1 *Signal* lepton and ≥ 2 *Signal* photons
$\Delta R_{\gamma\gamma} > 0.4, \Delta R_{l\gamma} > 0.4$
$E_T^{miss} > 25$ and $m_T^W > 40$ GeV
No additional *Preselect* same-flavour lepton
No additional opposite-flavor *Baseline* lepton
$Z\gamma$ veto cuts: $p_T^{l\gamma\gamma} > 30$ GeV, and 81 GeV $< m_{l\gamma\gamma}, m_{l\gamma 1}, m_{l\gamma 2} < 100$ GeV
b-jet veto on jets with $p_T > 20$ GeV and $\lvert\eta\rvert < 2.4$
$JVT > 0.5$ for jets with $20 < p_T < 60$ GeV and $\lvert\eta\rvert < 2.4$

Table 4.1: Summary of the Signal Region selection criteria [23].

triggers used in the control region are similar to those used to identify events in the Signal Region.

The observed and predicted number of events in both the SR and the CR are plotted in Figure 4.3. The observed number of events is statistically consistent with the predicted number of events. The observed and predicted number of events in bins of $p_T^{\gamma 1}$ is also shown in Table 4.2. The latter includes the values of the distribution constructed for this thesis and those of the distribution constructed for the original analysis. Both are in agreement, demonstrating the ability to reproduce the published results.

4.5 Studies of $pp \to W\gamma\gamma$ Sensitivity to Different Dimension-8 Operators

Prior to performing a quantitative analysis to constrain the effects of new physics, it is essential to characterize the sensitivity of the $pp \to W\gamma\gamma$ process to the different Effective Field Theory (EFT) operators shown in Table 2.1. This section focuses on identifying which operators predict the largest deviation in the expected number of events compared to the SM expectations. The case where the number of events deviates significantly from the SM prediction indicates that the specific operator is a sensitive probe for determining whether BSM physics contributes to the observed cross-section and for constraining the coupling of new physics to the SM. This step also provides valuable information to identify the relevant energy scales at which EFT operators

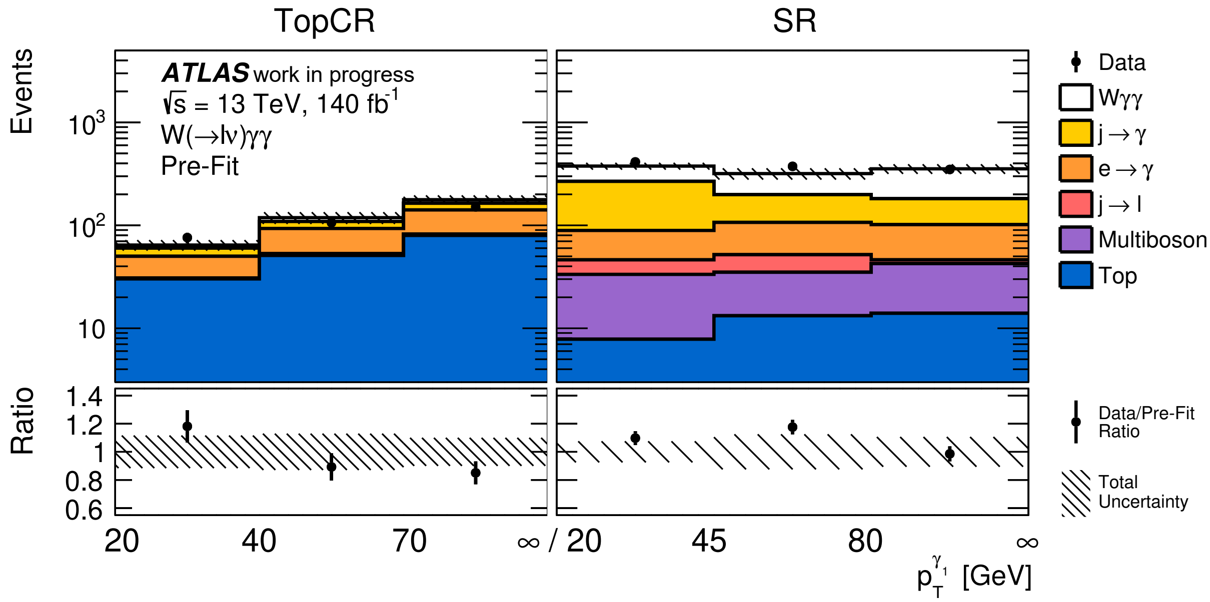

Figure 4.3: Data and pre-fit yields for Top Control Region and Signal Region of $W\gamma\gamma$ as a function of leading photon transverse momentum ($p_T^{\gamma 1}$) kinematic distribution, each with three bins. Pre-fit values refer to the number of events before the likelihood fit described in later sections. The error bars on the data indicate its statistical uncertainty. The dashed bands represent the total uncertainty on the predicted number of events. For this visual representation, theoretical, statistical, and systematic uncertainties, as described in [23], are combined in quadrature as an approximation, assuming all sources of uncertainty are fully uncorrelated. In the full analysis, correlations between uncertainties are properly accounted for where necessary. The bottom panels show the ratio of the observed to predicted number of events.

dominate. Appendix A presents all technical aspects on how the EFT Lagrangian in Equation 2.6 can be treated as a sum of amplitudes and then related to cross-section (Equation 2.5) and number of events (Equation 3.3).

Theoretical predictions of the number of events expected with the addition of different EFT operators are obtained using the MadGraph5 and Pythia8 generators [25]. The simulated samples are generated with an arbitrary coupling strength of $f/\Lambda^4 = 9 \times 10^{-11}$ GeV^{-4}. Simulated number of events can be reweighted to explore the effect of different coupling strengths. Figure 4.4 shows the predicted leading photon transverse momentum ($p_T^{\gamma 1}$) distributions for all relevant T-type dimension-8 operators with coupling strengths of $f/\Lambda^4 = 1$ TeV^{-4} and 10 TeV^{-4}. For each operator, the upper panel shows a binned distribution of the expected number of events for the SM and the SM plus EFT contributions for two different coupling strengths. The lower panel shows the ra-

	$p_T^{\gamma 1}$ Region [GeV]				
Event Type	[20, 45]	[45, 80]	[80, ∞]	Total	Published
$W\gamma\gamma$ (e, μ, τ)	109	119	173	401	401 ± 20
j $\rightarrow \gamma$	215	120	86	421	420 ± 48
e $\rightarrow \gamma$	43	55	55	153	153 ± 11
j $\rightarrow$ l	12	17	3	32	35 ± 10
Multiboson	26	22	29	77	76 ± 13
Top	7	13	14	34	35 ± 4
Predicted Total	412	346	360	1118	1120 ± 55
Observed Data	413	374	349	1136	1136

Table 4.2: Observed and predicted number of events in bins of $p_T^{\gamma 1}$ in the $W\gamma\gamma$ Signal Region defined by the selection criteria presented in Table 4.1. The number of events obtained in the analysis presented in this thesis is compared to the number of events published in [23]. An additional source of background not listed in the table arises from events where one or both photons originate from a vertex different from the primary vertex. This source of background is referred to as pileup background and is estimated in [23] as contributing less than 1 % of the total predicted number of events in the signal region. For the analysis presented in this thesis, this source of background is therefore neglected. Consequently, the total number of events slightly differs from those published in [23].

tio to SM. Operators that produce larger deviations from the SM distributions, especially at higher $p_T^{\gamma 1}$ values, indicate greater sensitivity to potential new physics effects encoded by the EFT. As such, the comparison presented in this figure helps conclude that the $W\gamma\gamma$ analysis is most sensitive to operators $\mathcal{O}_{T,5}$ and $\mathcal{O}_{T,6}$. In contrast, for equivalent coupling strengths of $f/\Lambda^4 = 1$ TeV^{-4} and 10 TeV^{-4}, M-type dimension-8 operators only lead to a change in the predicted number of events of less than 1 %. Therefore, it can be inferred that the $pp \rightarrow W\gamma\gamma$ process has little sensitivity to M-type operators.

4.6 Constraints on Dimension-8 Operator Coefficients

A likelihood-based scan of the parameter space associated with the anomalous quartic gauge couplings (aQGCs) is performed to constrain the coefficient of each operator contributing to the $pp \rightarrow W\gamma\gamma$ process. This chapter outlines the statistical framework used to quantify the sensitivity

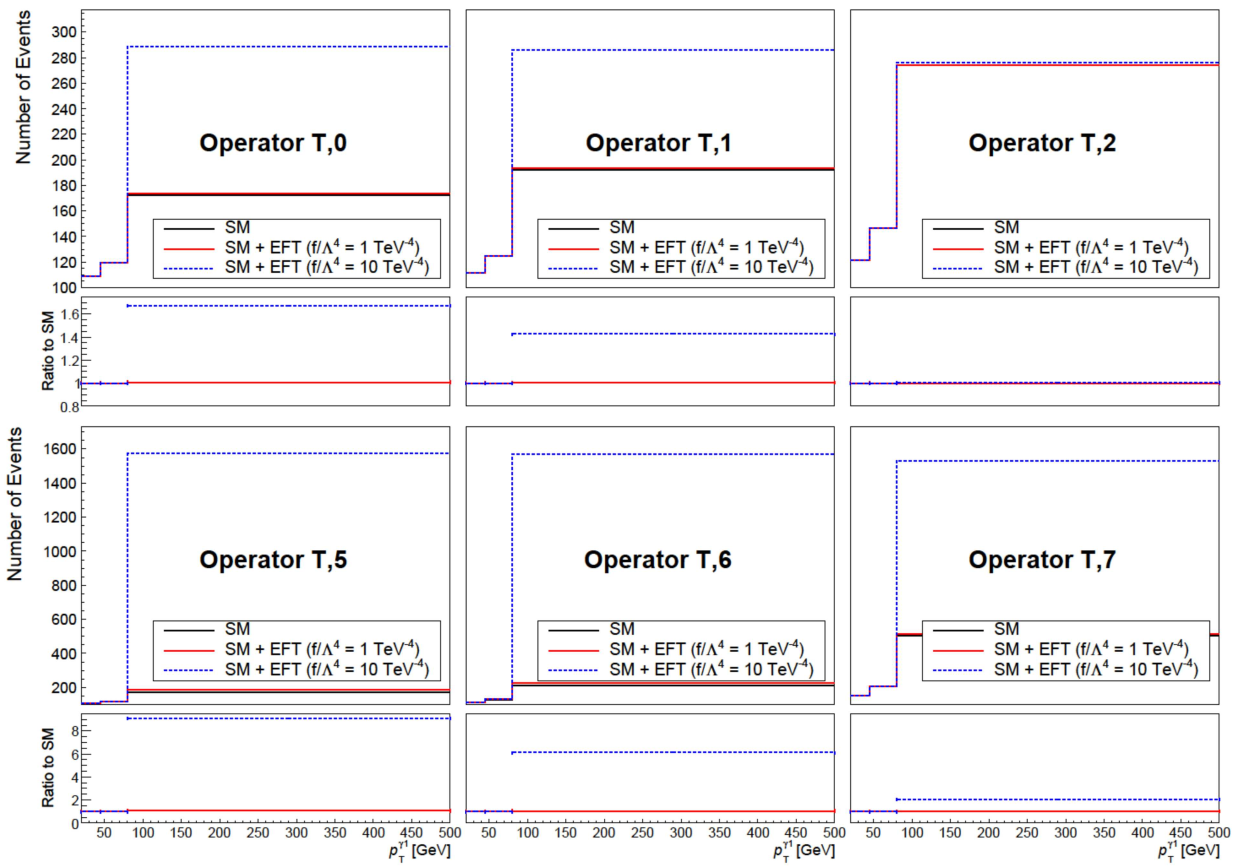

Figure 4.4: Number of $W\gamma\gamma$ evens in the Signal Region predicted by the SM and with the addition of T-type dimension-8 operators as a function of leading photon transverse momentum ($p_T^{\gamma 1}$). SM-only leading photon transverse momentum ($p_T^{\gamma 1}$) distributions are shown as a solid black line. The SM plus EFT distributions are shown in dashed red and blue, for coupling strengths 1 TeV^{-4} and 10 TeV^{-4}, respectively. The ratios are taken by dividing SM+EFT by the SM. Ratios that deviate from 1 indicate a greater sensitivity to new physics.

to Beyond Standard Model (BSM) effects using the process of interest. The methods presented in this chapter are taken from [26].

The probability of observing data given a hypothesis H is given by $P(\text{data}|H)$. Given the frequentist nature of the analysis, the probability for a fixed set of data points is called the likelihood. The likelihood function is defined as the probability of observing the data given a set of parameters $\vec{\theta}$, and is written as $\mathcal{L}(\vec{\theta})$.

4.6.1 Likelihood Model

The total likelihood is built from a binned $p_T^{\gamma 1}$ distribution assuming Poisson-distributed event counts in each bin. For this analysis, the likelihood function $\mathcal{L}$ can be written as a product of Poisson distributions:

$$\mathcal{L} = \prod_{i}^{N_{bins}} \prod_{r}^{N_{reg}} P(n_{i,r} | S_{i,r}(\vec{c}, \alpha_{\text{top}}, \vec{\theta}) + B_{i,r}(\alpha_{\text{top}}, \vec{\theta})) \tag{4.1}$$

where N_{bins} is the number of bins of the kinematic distribution, N_{reg} is the number of regions (in this analysis, the regions used are the Signal Region SR and Top Control Region CR), P represents a Poisson probability distribution, $n_{i,r}$ is the number of observed events (measurement) in bin i and region r, $S_{i,r}$ is the predicted number of signal events in bin i and region r given by the SM Lagrangian combined with additional higher order operators and their associated set of unknown coupling strengths $\vec{c}$, and $B_{i,r}$ is the predicted number of background events in bin i and region r. The symbol α_{top} is the top normalization factor used to estimate the number of background events from processes with a top quark in their final state. The symbol $\vec{\theta}$ are nuisance parameters associated with uncertainties in the prediction of backgrounds. Nuisance parameters representing the experimental and theoretical uncertainties are constrained using a Gaussian probability density function, while statistical uncertainties are constrained with a Poisson probability distribution. Factors $\vec{c}$, α_{top}, and $\vec{\theta}$ are allowed to float in the fit.

This likelihood function encodes the agreement between prediction and measurement, e.g values of $\vec{c_i}$ that result in a number of events close to n_i. The parameters of interest in this likelihood study are the Wilson coefficients, or the EFT coupling strength, $\vec{c} = \frac{f_j}{\Lambda^4}$, and the top CR normalization parameter α_{top}.

4.6.2 Likelihood-Based Parameter Limit Estimation

The likelihood scan procedure allows exploration of different coupling values associated with different higher-dimensional EFT operators by identifying which values are more consistent with data. This is accomplished by evaluating, at each point in the parameter space, how well the predicted distributions match the observed event counts across the multiple bins of the kinematic distribution.

The best fit value of parameters $\vec{c}$ and α_{top}, and all nuisance parameters $\vec{\theta}$ are estimated using the Maximum Likelihood Estimator method [26], which finds the values that make the observed data most probable under the constructed model:

$$-\frac{\partial \mathcal{L}}{\partial \vec{c} \partial \alpha_{\text{top}} \partial \vec{\theta}} = 0 \tag{4.2}$$

Additionally, a frequentist significance test is used to derive confidence intervals on statistically allowed values of Wilson coefficients $\vec{c} = \frac{f}{\Lambda^4}$. The significance test is based on the profile likelihood ratio defined as:

$$\lambda = \frac{\mathcal{L}(\vec{c}, \alpha_{\text{top}}, \hat{\hat{\vec{\theta}}})}{\mathcal{L}(\hat{\vec{c}}, \hat{\alpha_{\text{top}}}, \hat{\vec{\theta}})} \tag{4.3}$$

where $\hat{\hat{\vec{\theta}}}$ are the values of nuisance parameters which maximizes $\mathcal{L}$ for a given value of $\vec{c}$ and α_{top}, and $\hat{\vec{c}}$, $\hat{\alpha_{\text{top}}}$ and $\hat{\vec{\theta}}$ are the estimators that maximize $\mathcal{L}$ found using Equation 4.2. The profile likelihood ratio λ is close to 1 when the observed data agrees well with the hypothesized value.

A test statistic can then be defined to quantify the level of compatibility between the prediction and the measured data. The profile likelihood ratio test statistic is defined as:

$$t = -2\ln(\lambda) = -2\ln \frac{\mathcal{L}(\vec{c}, \alpha_{\text{top}}, \hat{\hat{\vec{\theta}}})}{\mathcal{L}(\hat{\vec{c}}, \hat{\alpha_{\text{top}}}, \hat{\vec{\theta}})} \tag{4.4}$$

Exploiting logarithmic properties, Equation 4.4 can be rewritten as:

$$t = -2[\ln \mathcal{L}(\vec{c}, \alpha_{\text{top}}, \hat{\hat{\vec{\theta}}}) - \ln \mathcal{L}(\hat{\vec{c}}, \hat{\alpha_{\text{top}}}, \hat{\vec{\theta}})] = -2\Delta \ln \mathcal{L} \tag{4.5}$$

such that the test statistic is 0 when the data is in perfect agreement with the model, and its value grows with incompatibility between the hypothesized value and the observed data. Under Wilks' theorem [27], in the large statistics limit, the test statistic t tends to a χ^2 distribution, and p-values can be used to determine confidence intervals.

In general, the p-value is obtained by integrating the probability density $f(t)$:

$$p = \int_{t_{\text{obs}}}^{\infty} f(t)dt \tag{4.6}$$

The area under the curve captures the probability associated with the tail of the distribution beyond the measured test statistic value, which represents the probability of obtaining a value greater than the observed value t_{obs} in repeated experiments. For example, a 95 $\%$ Confidence Interval (CI) for $\vec{c}$ consists of those values of $\vec{c}$ for which the p-value is 0.05. Assuming the probability distribution of the test statistic t tends towards a χ^2 probability distribution in the large-sample limit, the 95 $\%$ percentile corresponds to a test statistic value of 3.84.

4.6.3 Likelihood Model Implementation

The methods outlined before are all implemented in the EFT-Fun tool [28]. EFT-Fun is a Python-based computational fitting tool designed to facilitate analyses within an Effective Field Theory framework. It allows users to construct, manipulate, and evaluate EFT operators and their effects on scattering amplitudes.

In this thesis, this tool is used by writing configuration files specific to the $W\gamma\gamma$ analysis and then running the EFT-Fun algorithm to perform likelihood scans and fits.

4.7 Results

The likelihood method outlined in the sections before has been implemented to perform preliminary limit setting on the operators of interest, namely $\mathcal{O}_{T,5}$ and $\mathcal{O}_{T,6}$.

To conduct the initial likelihood scans, a model was constructed taking into account 1 $\%$ pruning. So, systematic uncertainties that resulted in less than a 1 $\%$ deviation from the nominal value

Source of uncertainty	Impact (%)
j$\rightarrow \gamma$ data-driven background estimate	12.5
Photon efficiency	4.5
Other data-driven background estimates	3.5
Background Theoretical Uncertainties	3.0
Simulation Statistical Uncertainties	2.7
Signal Theoretical Uncertainties	2.6
Jet Efficiency and Calibration	2.4
Top normalization	2.3
Pileup reweighting	1.6
Muon Efficincy and Calibration	1.4
MET Calibration	1.3
Luminosity	1.0
Electron and Photon calibration	0.7
Flavour tagging efficiency	0.6
Total (Syst)	15
Total (Stat)	8.3
Total	17

Table 4.3: Major sources of uncertainty and their relative contribution to the total uncertainty on the measured fiducial cross-section. All values are taken from the analysis paper [23].

were considered negligible and removed from the analysis. Table 4.3, taken from [23], shows the different sources of uncertainties and their impact percentage. The most significant uncertainties arise from sources of uncertainty with a large impact value. The impact value of an uncertainty quantifies how much a specific source of uncertainty shifts the estimated value of a model when the uncertainty is varied within its allowed range. Accordingly, the uncertainties pruned for the results presented in this thesis include Luminosity, Electron and Photon calibration efficiencies, and Flavour tagging efficiency.

This analysis plans to be included within an ATLAS-wide combination for exploring the nature of aQGC in different final states.

Likelihood Scans

One-dimensional (1D) scans of the likelihood parameter space have been performed for the operators $\mathcal{O}_{T,5}$ and $\mathcal{O}_{T,6}$, as shown in Figures 4.5(a) and 4.5(b), respectively. In these scans, only one operator coefficient is left floating as a fit parameter. Each operator coupling is varied indepen-

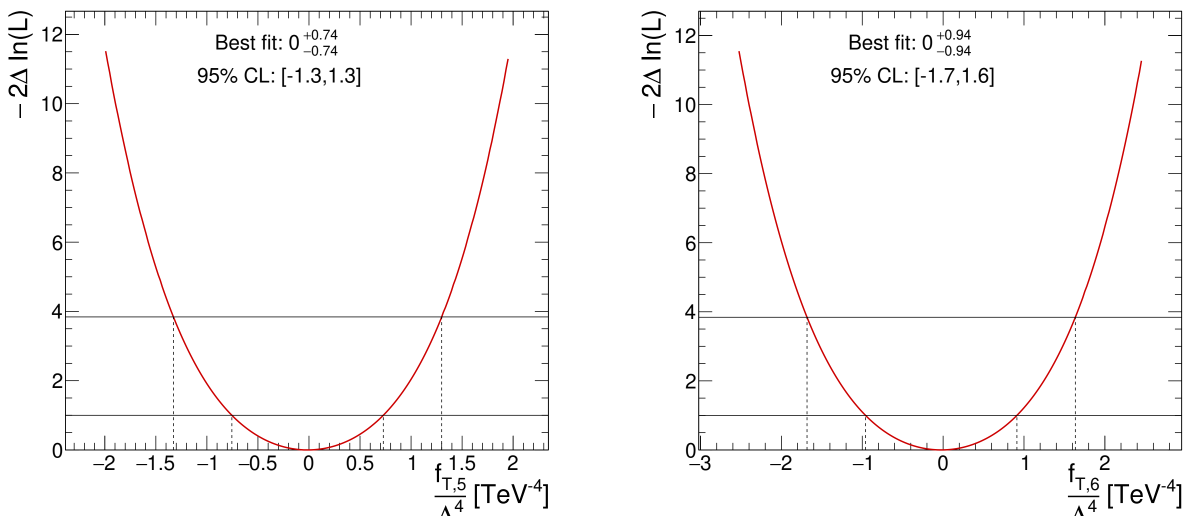

Figure 4.5: Distribution of the test statistic $t = -2\Delta\ln(\mathcal{L})$ as a function of coupling $\frac{f_j}{\Lambda^4}$ for operators (a) $\mathcal{O}_{T,5}$ and (b) $\mathcal{O}_{T,6}$. The vertical dash lines indicate the coupling values at which the test statistic is at a value of 1, corresponding to a 68 % CI, and 3.84, corresponding to a 95 % CI. The best-fit coupling value that minimizes the likelihood is also shown at the top of each plot.

dently while all other operator coefficients are fixed to zero. The resulting plot is a parabola given by Equation 4.4 with 95 % confidence intervals extracted from the coupling values corresponding to a $t = -2\Delta\ln\mathcal{L}$ value of 3.84. The 1D results are shown below in Table 4.4:

	95 % Confidence Interval [TeV $^{-4}$]
$\frac{f_{T,5}}{\Lambda^4}$	[-1.3, 1.3]
$\frac{f_{T,6}}{\Lambda^4}$	[-1.7, 1.6]

Table 4.4: The 1D 95% confidence interval on the coupling coefficient for operators $\mathcal{O}_{T,5}$ and $\mathcal{O}_{T,6}$.

Additionally, a two-dimensional (2D) scan of the likelihood parameter space between operators $\mathcal{O}_{T,5}$ and $\mathcal{O}_{T,6}$ has been performed by simultaneously treating both of their respective coupling coefficients as free parameters in the fit. In addition to 1D scans, 2D scans are used to investigate potential correlations and to set combined limits by exploring the merged likelihood space. For example, in the case of strong parameter correlation, stringent bounds on one operator, possibly obtained from another analysis, can enhance the constraints on the other. Figure 4.6 shows the resulting test statistic $t = -2\Delta\ln(\mathcal{L})$ as a function of the coupling coefficients for $\mathcal{O}_{T,5}$ and $\mathcal{O}_{T,6}$. Assuming that the test statistic function t follows a χ^2 distribution, for two degrees of freedom, the contours of the 2D scan are 95 % for $t = -2\Delta\ln(\mathcal{L}) = 5.99$ and 68 % for $t = -2\Delta\ln(\mathcal{L}) = 2.28$. The resulting 95% confidence intervals on the relevant coupling coefficients are summarized in Table 4.5.

	95 % Confidence Interval [TeV $^{-4}$]
$\frac{f_{T,5}}{\Lambda^4}$	[-1.6, 1.6]
$\frac{f_{T,6}}{\Lambda^4}$	[-2.0, 2.0]

Table 4.5: The 2D correlated 95% confidence interval on the coupling coefficient for operators $\mathcal{O}_{T,5}$ and $\mathcal{O}_{T,6}$.

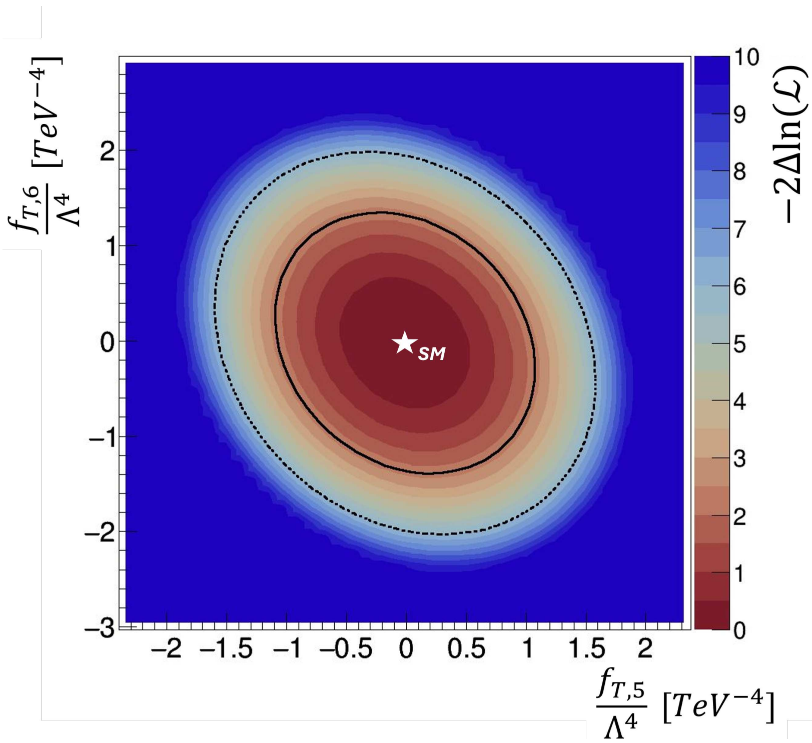

Figure 4.6: Distribution of the test statistic $t = -2\Delta\ln(\mathcal{L})$ as a function of coefficients $\frac{f_{T,5}}{\Lambda^4}$ and $\frac{f_{T,6}}{\Lambda^4}$. The colour map indicates the depth of a 2D parabola. Contours represent the confidence intervals at 68 % and 95 %. The scan highlights the correlation between the two parameters and provides a comparison to the SM prediction shown by the white star.

The confidence intervals derived from the 1D and 2D likelihood scans differ primarily due to the way parameter correlations are treated in each method. In the 1D scans, each parameter is varied independently while the others are fixed to zero. This approach isolates the effects of a single operator, enabling constraints to be set under the assumption that no other contributions are present. However, this approach does not account for correlations between parameters and thus narrows the parameter space. Essentially, the parameter space is reduced, allowing for tighter limits.

In contrast, 2D likelihood scans allow both $\mathcal{O}_{T,5}$ and $\mathcal{O}_{T,6}$ to vary simultaneously, thereby capturing their joint behaviour and possible interference effects. This leads to a more complete exploration of the joint parameter space and typically yields broader confidence regions. The elliptical shape of the resulting 2D likelihood contours and the looser constraints compared to the 1D scans indicate a non-negligible correlation between the two parameters of interest.

Both the 1D and 2D scans provide valuable results and insights: the 1D scans offer a simplified interpretation where only one operator is active, while the 2D scans reflect a more realistic picture consistent with an extended Standard Model Lagrangian that includes all relevant EFT operators and their potential interferences. Consequently, the 2D scan results are better suited for drawing robust conclusions about the full parameter space allowed by the observed data.

4.8 Comparison to Existing Constraints

It is important to place this analysis in context by comparing the results with existing limits on effective field theory parameters reported by other studies. Figure 4.7 presents a summary of constraints derived from various diboson and triboson final states studied to probe the same set of operators. Note that the confidence intervals reported in Figure 4.7 are those obtained from a fit to experimental data.

Focusing on the two operators of interest ($\mathcal{O}_{T,5}$ and $\mathcal{O}_{T,6}$), the one-dimensional confidence intervals obtained in this thesis are found to be comparable to other existing limits, demonstrating

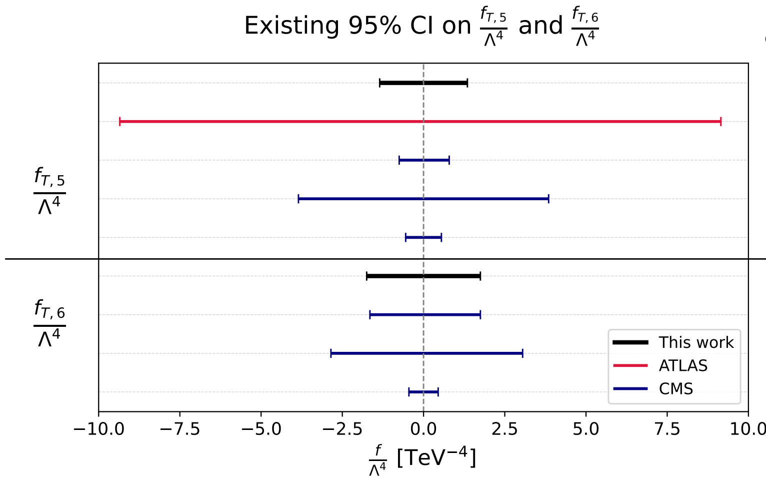

Channel	Limits	$\sqrt{s}$	$\int \mathcal{L}dt$
$W\gamma\gamma$	[-1.3e+00, 1.3e+00]	13 TeV	140 fb^{-1}
$Z\gamma\gamma$	[-9.3e+00, 9.1e+00]	8 TeV	120.3 fb^{-1}
$Z\gamma$	[-7.0e-01, 7.4e-01]	13 TeV	135.9 fb^{-1}
$W\gamma$	[-3.8e+00, 3.8e+00]	8 TeV	119.7 fb^{-1}
$W\gamma$	[-5.0e-01, 5.0e-01]	13 TeV	135.9 fb^{-1}
$W\gamma\gamma$	[-1.7e+00, 1.7e+00]	13 TeV	140 fb^{-1}
$Z\gamma$	[-1.6e+00, 1.7e+00]	13 TeV	135.9 fb^{-1}
$W\gamma$	[-2.8e+00, 3.0e+00]	8 TeV	119.7 fb^{-1}
$W\gamma$	[-4.0e-01, 4.0e-01]	13 TeV	135.9 fb^{-1}

Figure 4.7: Different diboson and triboson final states used to set 95 % Confidence Intervals on quartic gauge couplings (aQGCs) for operators $\mathcal{O}_{T,5}$ and $\mathcal{O}_{T,6}$. The line color corresponds to which experiment presented the result: blue for CMS and red for ATLAS. This work, done with ATLAS data, is shown in black. Additional analysis information is also shown: center-of-mass energy $\sqrt{s}$ and integrated luminosity $\int \mathcal{L}dt$. Comparison summarized for relevant operators from [29].

competitive sensitivity and complementarity with other previous work, with the possibility of setting tighter constraints on the EFT parameter space. Similarly, the two-dimensional confidence intervals obtained in this thesis are found to be consistent with previous results. While the full impact of parameter correlations requires further study, 2D scans give insight into the interference between operators. Given the competitive sensitivity observed, such scans are useful in the context of a larger ATLAS-wide combination study. In that setting, 2D scans and strong correlations between parameters can be exploited to set even more stringent limits on operators.

In conclusion, this analysis demonstrates that the $W\gamma\gamma$ channel represents a valuable and sensitive probe to new physics phenomena manifesting themselves in quartic gauge interactions through higher-dimensional EFT operators.

Chapter 5

Upgrade to the ATLAS detector for the High-Luminosity LHC

The previous chapters highlighted the crucial role of the LAr calorimeter sub-detector in the identification of photons for reconstructing events like $W\gamma\gamma$. Now, the second part of this thesis focuses on the work conducted in the context of the Phase-II electronics upgrade of the ATLAS LAr detector for the High-Luminosity LHC.

The proposed high-luminosity upgrade of the CERN Large Hadron Collider presents an opportunity for the ATLAS experiment to significantly extend its physics program and study even rarer events. At the same time, it presents new technical challenges that need to be addressed.

5.1 The High-Luminosity LHC

The High-Luminosity Large Hadron Collider (HL-LHC) project is an ambitious upgrade to the LHC. It aims to improve the performance of the LHC in order to increase the potential for discoveries after 2030 [30]. The objective is to increase the instantaneous luminosity by a factor of 5-7.5 and the integrated luminosity by a factor of 10 beyond the nominal LHC design values. An increase in the instantaneous luminosity will increase the number of collisions per bunch crossing from approximately 20 to 200 [20]. The new configuration will rely on a number of key innovations that push accelerator technology beyond its present limits, with the goal of sustaining and extending the LHC discovery potential. The HL-LHC will increase the mass reach in the search for new particles, substantially improve precision measurements, and will also greatly extend the potential to study the properties of the Higgs boson [30].

In order to meet the experimental challenges of unprecedented proton-proton luminosity, the experiments at the LHC ring need to address the aging state of the detectors and improve the ability to isolate and measure the products of collisions in a complex environment [20]. All hardware changes needed to enable the luminosity upgrade will take place during one long shutdown around 2026-2030, with some initial modifications already done in 2019-2020 [31].

The basic goal of the upgrades to ATLAS is to maintain or improve the excellent performance of the detector in terms of efficiency, resolution, and background rejection for all the physics objects used in the analysis of the data [20]. The main challenges that must be addressed are radiation damage to the detectors from the high integrated luminosity and the high particle flux that comes from high instantaneous luminosity. Additionally, the larger event sizes will be a challenge for the trigger and Data AcQuisition (DAQ) systems, which require a significant extension of their capacity and design [32]. In the interest of this thesis, this section will only outline the upgrades to the Liquid Argon Calorimeter.

5.2 Upgrade to the Liquid Argon Calorimeter

With the proposed HL-LHC operating conditions, the current Liquid Argon readout system cannot meet radiation and data processing demands. A new readout architecture is essential to maintain and improve sensitivity. Additionally, the upgrade of the LAr readout electronics is necessary for the LAr detector to meet the ATLAS physics goals in the demanding conditions of the HL-LHC.

The upgrades to the LAr detector include new demands from the trigger and DAQ upgrades that motivate a redesign of the LAr readout architecture with stringent requirements on the performance of the electronics chain and improved radiation tolerance of all front-end components [32]. New

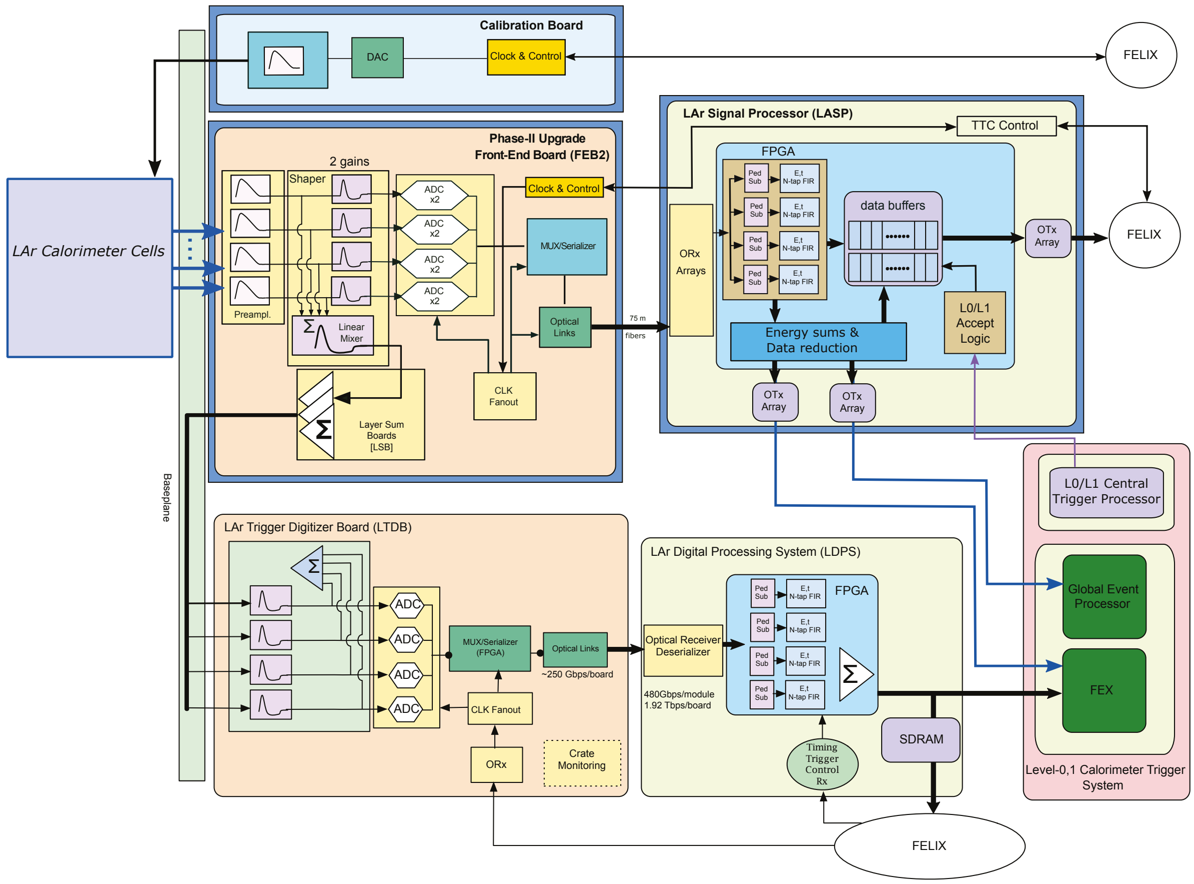

Figure 5.1: Schematic block diagram of the LAr calorimeter readout architecture for the Phase-II upgrade [20].

trigger requirements, in terms of rate, latency, and buffering capacity, imply a revision of the readout electronics architecture towards a free-running scheme where all data is digitized and sent off-detector [20]. Additional requirements on the readout system characteristics include dynamic range, linearity, noise, and analog pulse shaping time. For this thesis, the focus is solely on the new off-detector electronics, which will be located outside the detector cavern and are responsible for data handling once data is digitized on-detector.

5.3 New Readout Architecture for HL-LHC

Figure 5.1 shows a complete schematic of the Phase-II readout electronics. Most notably, the LAr readout electronics include the on-detector Front-End Boards (FEB2s), the off-detector Liquid

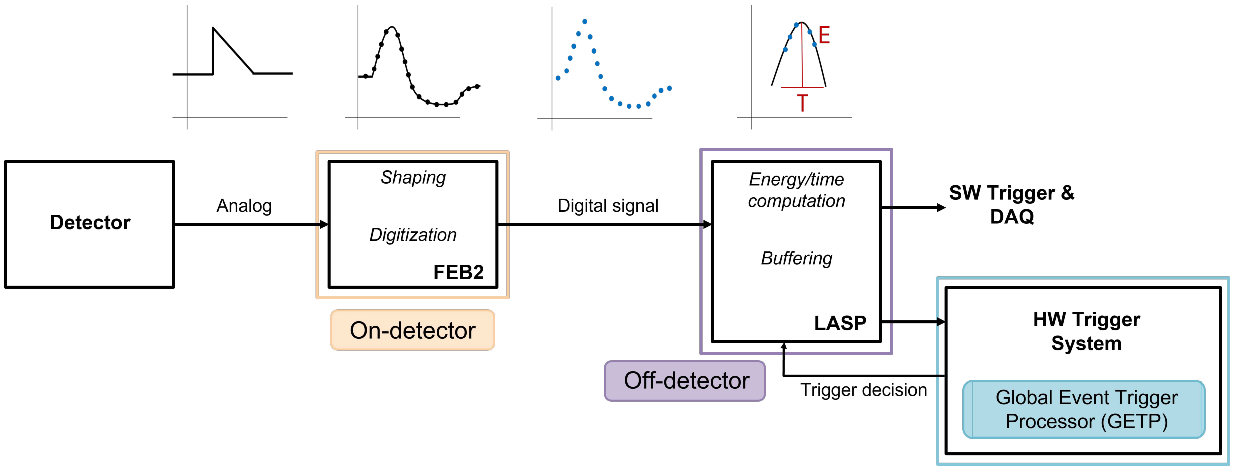

Figure 5.2: Flow diagram of the new liquid argon readout chain, highlighting the main components of the readout electronics and their functionality.

Argon Signal Processors (LASPs), among some other boards and systems key for the electronics chain. The trigger system, which operates alongside the readout system, includes several key components, notably the Calorimeter Trigger System, which is equipped with the Global Event Processor.

A functional overview of the new readout chain is highlighted in Figure 5.2. The front-end boards are responsible for amplification, pulse shaping, digitization, and transmission to the off-detector electronics. Each FEB2 board will handle up to 128 channels coming from 182,468 calorimeter cells. Each LASP FPGA will be able to process up to 3×128 channels. Taking into account channel mapping to make sure that FEB2s from the same LAr subsystem are sent to the same LASP board, the system will have a total of 364 LASP boards required to read out the entire LAr system [20]. The analog signal from each calorimeter cell is digitized at the bunch crossing rate of 40 MHz. Then, the outputs from the Analog to Digital Converters (ADCs) are serialized and sent via optical fibres to the off-detector LASP system. Off-detector, the LASPs process digitized waveforms, select a gain, implement a digital filtering algorithm, interface with the trigger and data acquisition systems, and buffer the data while awaiting a trigger decision. Each LASP processing unit takes inputs from up to 384 calorimeter cells [20]. The Global Event Trigger Processors (GETP) in the Trigger System receive energies from calorimeter cells which pass a given threshold relative to the total noise expected in each cell [33]. Finally, relevant data, upon receiving a positive trigger system decision, is sent to the data acquisition system.

5.4 Overview of the Liquid Argon Signal Processor Boards

The LASP board design is based on the Advanced Telecommunications Computing Architecture (ATCA) [20]. Additionally, the LASP units require a high input and output bandwidth and flexible programming of data handling, digital filtering, and data reduction algorithms [20]. Therefore, Field Programmable Gate Arrays (FPGAs) will be used as the main processing units. The LASP system will be compatible with the ATLAS DAQ and trigger architectures at the HL-LHC. A prototype board is currently under development using Intel Agilex-Family FPGAs [20].

The main building blocks of a LASP board will be two FPGA processing units mounted on a Printed Circuit Board (PCB) and connected via high-speed links to electro-optical converters. In the final configuration, each LASP FPGA will receive inputs from 3 FEB2 boards. The PCB board design features high density, high speed, complex signal mapping, with long signal tracks and relatively high power consumption. The boards will have to operate with virtually no problem for over 10 years. [20].

A pre-prototype board available at McGill during some of the duration of this thesis is shown in Figure 5.3. This figure highlights the main components of the LASP board as described above, namely, two FPGAs, here covered with heat sinks in copper, optical connections, a power supply region with capacitors, and JTAG and USB connections.

5.5 Data Transfer Tests

Tests were conducted to validate the data transfer between a LASP-like device and a Global Event Trigger Board prototype at the design maximum data rate of 25.78 Gbps. This chapter presents the development, implementation, and results of tests carried out at the Brookhaven National Lab in December 2024. High-bandwidth and low-latency data transfers were successfully achieved

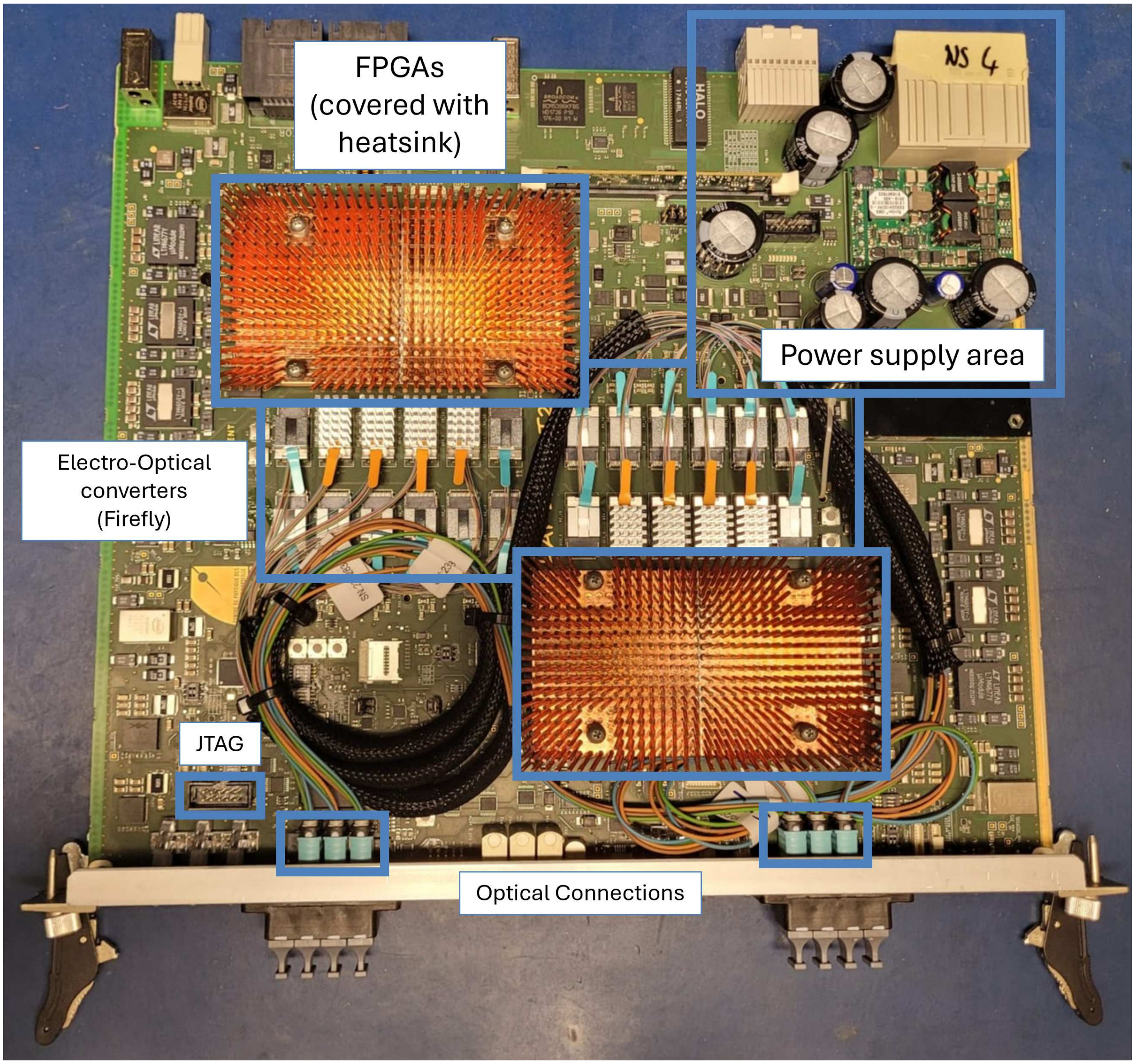

Figure 5.3: Pre-prototype LASP board T2 available at McGill with main components labeled. These include the two FPGAs (covered with copper heatsinks), the power supply area with capacitors, the JTAG connection, the optical connections, and the electro-optical converters (Firefly).

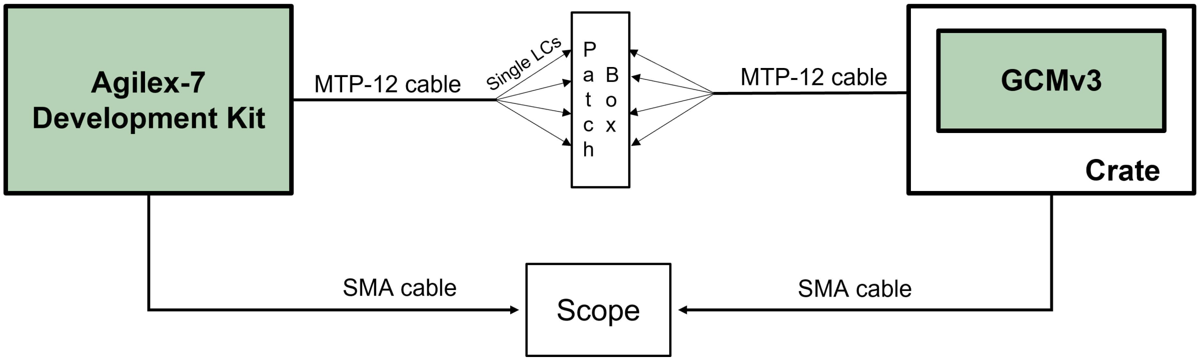

Figure 5.4: Schematic block diagram of the test setup highlighting main components and connections. Lucent Connectors (LC) are small form factor fiber optic connectors designed for high-speed communication.

between the two devices of interest. This work forms part of the broader LAr Calorimeter Phase-II Upgrade. Specifically, it addresses the current design status and challenges of a particular segment in the LAr calorimeter readout chain.

5.5.1 Hardware Setup

The hardware setup included an Intel Agilex-7 I-Series Evaluation Kit [34] acting as the LASP-like device on the transmitting side. On the receiving end, the Global Event Trigger Board is the version 3 GCMv3 board prototype [33]. The schematic diagram in Figure 5.4 shows both devices with relevant connections.

The Altera Agilex-7 FPGA I-Series Transceiver Development Kit is a comprehensive environment that includes both hardware and software, making it readily available for developing Agilex-7 FPGA I-Series designs. A top view of the Evaluation Kit is shown in Figure 5.5(a), and ready to be used in the lab in Figure 5.5(b). The board provides a wide range of peripherals and interesting features, including [34]:

- **DK-SI-AGI040EA FPGA Device**
  - 6 F-Tile transceiver capabilities
  - Dedicated General Purpose Transceiver (FGT) and High speed Transceiver (FHT) blocks

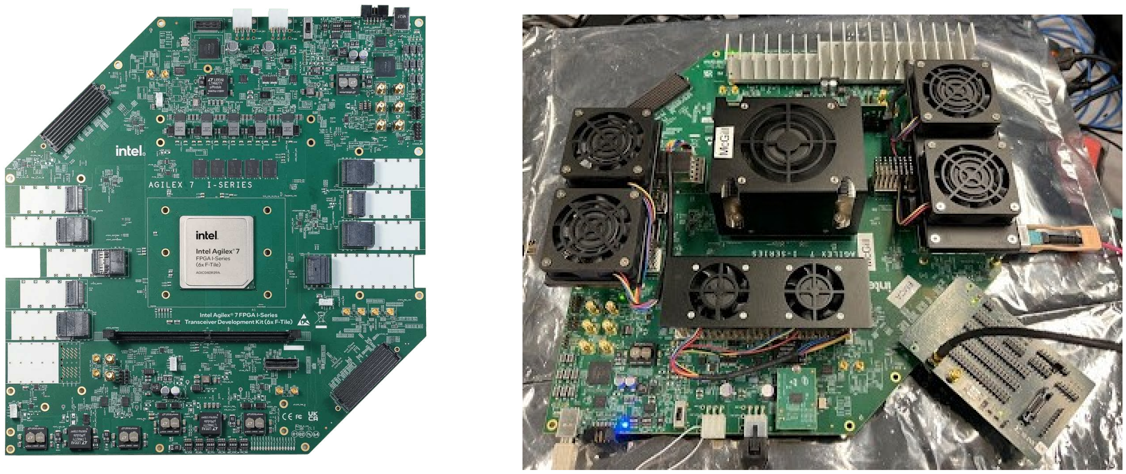

(a) (b)

Figure 5.5: (a) Top view of Agilex 7 FPGA I-Series Transceiver (6 × F-Tile) Development Kit, where the FPGA chip is mounted at the center of the PCB board. Refer to User Guide for a detailed Board Schematic [34]. (b) Lab use of Agilex Development Kit where fans cover the FPGA chip and all the QSFP modules. Additionally, heat sinks (top) and custom Xilinx XM105 FMC card (bottom right) are seen.

- **QSFP Modules:**
  - 4 × QSFP-DD
  - 1 QSFP-DD800
  - 3 × QSFP
  - Figure 5.5(b) shows module QSFP-100G-SR4-S by FS, an optical transceiver module designed for use in 100GBASE Ethernet using a wavelength of 850 nm via MTP-12 connector.
  - TX Power: -8.4 to 2.4 dBm
- **USB 2.0 Connector**
- **Ethernet Port**
- **On-board DDR4 32 Gb SDRAM**

Additionally, to have an SMA (SubMiniature version-A) connection from the Evaluation kit to an oscilloscope, a customized Xilinx XM105 FMC debug card was included, as shown in Figure 5.5(b).

On the receiving side, the Global Trigger Board relies on a unified hardware platform called the Global Common Module (GCM), hosting all firmware layers. For the Global Trigger, the

GCM has three main functionalities implemented through firmware: MUX (Data Aggregators and Multiplexer), GEP (Global Event Processor), and gCTPi (Global-to-CTP Interface) [33].

During the tests, version 3 of the GCM prototype was used. This third revision implemented the production target FPGA (Xilinx Versal Premium VP1802 [35]) to achieve a production-like hardware for testing. GCMv3 is an ATCA form factor card, which is the standard for all CERN electronic boards. This standard card features two large FPGAs and 20 FireFly optical modules [33]. These and other main components are shown in Figure 5.6 and highlighted below [33]:

- **Power Module:**
  - 1 PIM4328 / 1 BMR458 (-48V/12V)
  - 7 LTM4681 / 1 LTM4638 (POL rails)
- **Versal Adaptive System on Chips (SoCs):**
  - 1 Versal Premium VP1802 for MUX
  - 1 Versal Premium VP1802 for GEP/gCTPi
- **FireFly Modules:**
  - 1 T24 and 3 R24 for GEP/gCTPi
  - 2 T24, 3 R24 and 1 Y12 for MUX
- **GbE Ports:**
  - 1 for IPMC / 1 for MUX / 1 for GEP
- **USB-C Connector:**
  - 3 UARTs / 1 JTAG / 1 HSDP
- **2 $\times$ 16GB VLP DDR4 UDIMMs**
- **2 $\times$ SD Cards**
- **2 $\times$ Si5395A Clock Generators**
- **CERN IPMC [36]**

A 4 m optical fiber connection was used to link the boards across a total of four different links. Additionally, an oscilloscope was used to monitor GPIO (General-Purpose Input/Output) signals, allowing for the time-stamping of transmission and reception events. The connection to the oscilloscope was achieved using SMA coaxial cables. The overall setup is shown in Figure 5.7.

Figure 5.6: The GCMv3 prototype board with relevant components [33]. The blue tape secures cables close to the board to ensure proper insertion into the ATCA crate.

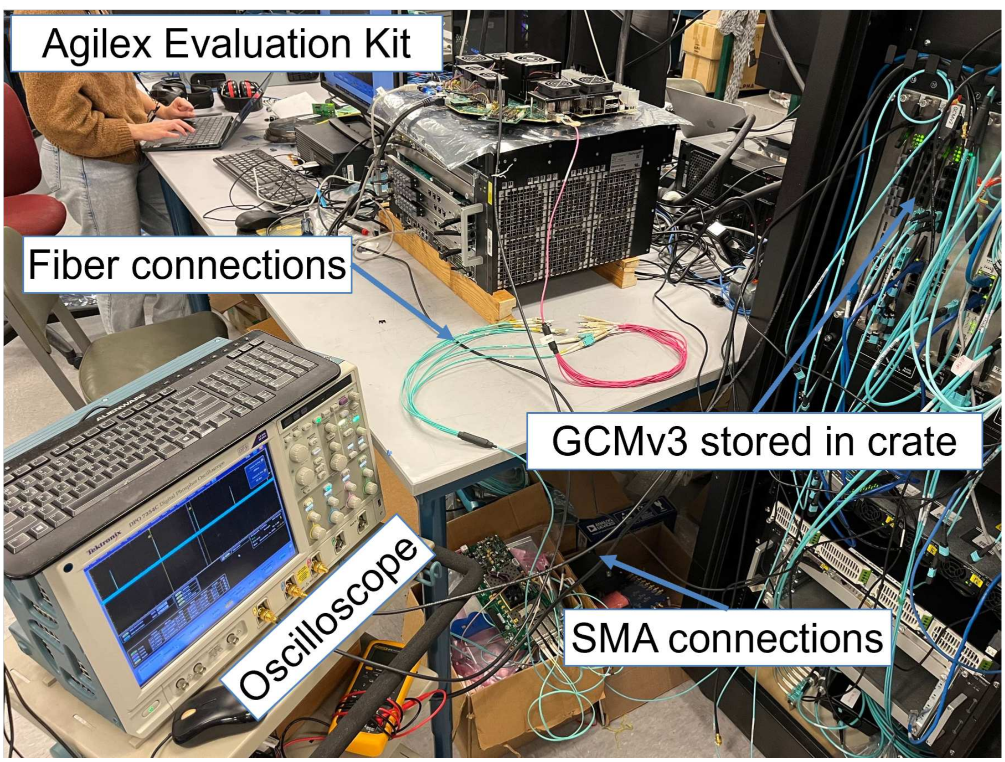

Figure 5.7: Lab setup for data transmission tests. Agilex-7 Development kit, oscilloscope, and GCMv3 board stored vertically in an ATCA crate. A 4 m optical fibre connection, as well as SMA connections to an oscilloscope are also visible.

5.5.2 Firmware Setup: Core1990 Implementation

The data transmission firmware written and implemented for the data transfer tests is based on the Core1990 protocol. Core1990 is a point-to-point communication framework developed by the Electronics Department of Nikhef (Amsterdam) with large experiments at CERN in mind [37]. It was designed to explore and publish an open-source protocol capable of handling high-speed data transmission with minimal overhead. It uses the royalty-free Interlaken protocol as its foundation but was adapted for use on both Intel Agilex and Xilinx Versal FPGAs.

The Interlaken protocol was invented in 2006 as an improvement to the protocols available at the time that only offered fixed configurations, limiting the ability of the designer to tailor the interface capacity to the intended application. Instead, the Interlaken protocol enables the design of a narrow, high-speed, channelized chip-to-chip packet interface. It is optimized for high bandwidth and reliable packet transfer. It is characterized by support for up to 256 communication channels, a simple control word structure to delineate packets, a continuous Meta Frame structure with programmable frequency to guarantee lane alignment, and a 64/67-bit data encoding [38].

The two fundamental structures of the Interlaken protocol are the data transmission format and the Meta Frame, both shown in Figure 5.8 [38]. The data transmission format is made up of data segmented in bursts, which are subsets of the original data packet [37]. Each burst is bounded by two control words: Start and End. This particular characteristic is optimized specifically for LAr. The two control words are put together into a single one called the Start/End Of Packet (SEOP) word. The size of the bursts is a user-configurable parameter [37]. By segmenting the data into bursts, the interface allows the interleaving of data from different channels, achieving low-latency operation. Furthermore, the Meta Frame encompasses a set of four unique control words, which are defined to provide lane alignment, scrambler, clock, and diagnostic information. Meta Framing runs in-band with data but uses the unique formatting of control words to distinguish it [38].

For LAr, Core1990 was implemented by using Start/End of Package (SEOP) words, minimizing the number of control words per data package. Furthermore, user data is packed into Burst Frames of size *BurstLength* + *SEOP*. A Meta Frame has size *MetaFrameLength*, including four

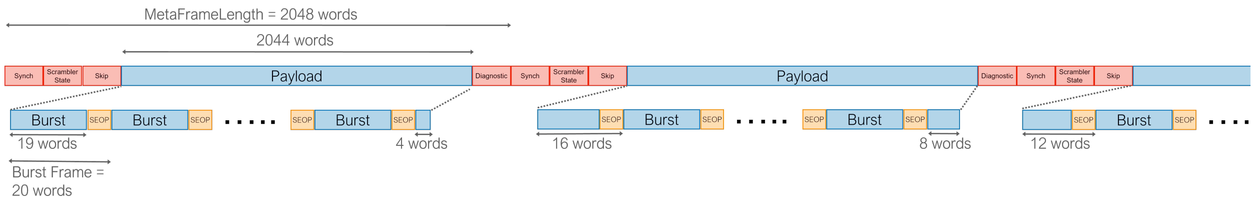

Figure 5.8: Meta Frame and payload structure of the Core1990 implementation for LAr. This example uses a burst length of 19 words.

meta framing control words. Figure 5.8 shows a package sample for a burst length of 19 words. A Meta Frame has a total of 2048 words including four control words, and a payload is constructed from bursts and SEOP words until filling up 2044 words.

Firmware built from the Core1990 logic was implemented by colleagues on both the transmitting and receiving ends. Figure 5.9 is a schematic diagram showing the firmware logic of each component. The Agilex-7 transmitting firmware includes a Core1990 IP Core composed of the Core1990 logic described in Section 5.5.2 along with a First-In-First-Out (FIFO) and a transmitting (TX) component. Along with this IP Core, the firmware features a data generator that supports configurable data rates and burst lengths, giving the user full control of the payloads. The firmware also operates at a single domain clock of 402.83 MHz, which is about 10 times the nunch crossing frequency of the LHC. Similarly, on the receiving (RX) side, the firmware is composed of the Core1990 logic along with a data checker, which validates data integrity. Furthermore, it is equipped with two synchronous accumulators to monitor transmission time and valid data. The first accumulator increases with every clock cycle, while the second accumulator increases with every valid data packet received. Then, bandwidth is calculated by taking the ratio of the two. This firmware also operates with a single clock domain at the same frequency of 402.83 MHz. Finally, both firmware implementations generate GPIO flags at the start and end of the Core1990 logic. These flags can be observed with the oscilloscope and are used to monitor the behaviour of the core logic, to monitor the integrity of the firmware, and to measure latency times.

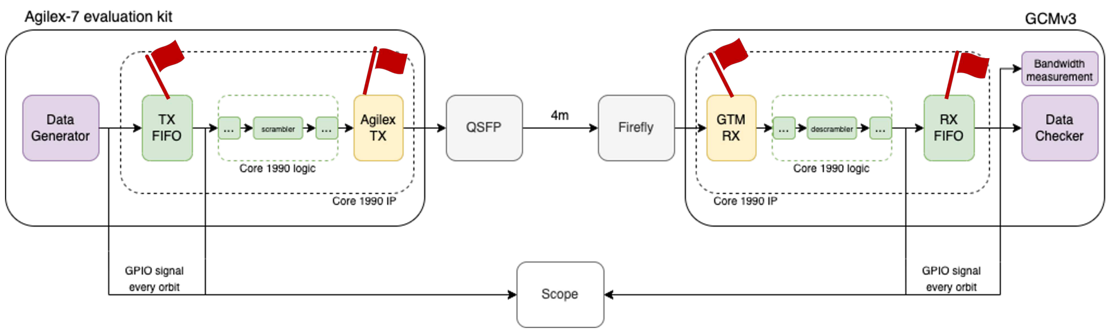

Figure 5.9: Schematic diagram of the firmware logic of the complete test setup.

5.6 Theoretical Predictions

Bandwidth

Bandwidth refers to the maximum theoretical capacity of a network connection, measured in gigabits per second (Gbps). Theoretical bandwidth coming from the Core1990 logic is evaluated by multiplying the maximum available bandwidth by different ratios that account for the effects of the data structure:

$$BW = 25.78 \text{ Gbps} \times \frac{64}{67} \times \frac{N}{N+1} \times \frac{2044}{2048} \tag{5.1}$$

where the maximum available bandwidth is not only the industry standard but also corresponds to 402.83 MHz $\times\, 64-$bits, the number of bits sent per clock cycle. Then, the ratio $64/67$ accounts for the encoding of a 64-bit payload with a 3-bit header, the term $N/(N+1)$ accounts for the effect of burst length plus one SEOP word, and finally, the ratio $2044/2048$ is the effect of the Meta Framing with a length of 2048 containing four meta control words.

For example, for a burst length of $N = 19$ words, Equation 5.1 yields a maximum possible data bandwidth of 23.35 Gbps. Now, to determine whether a combination of input data rate and transmission burst length is viable, the Core1990 bandwidth must be compared to the data rate from the data generator into the TX FIFO. If the data generator is sending data to the FIFO at a higher rate than the Core1990 IP Core can handle, the FIFO fills up and the data transfer is no longer efficient. For example, if the generated data rate is 8 words per 10 clock cycles, the bandwidth out of the data generator is 20.63 Gbps. This is slower than the Core1990 bandwidth calculated before, meaning that the FIFO will not fill up, and the chosen parameters are optimally functional. This comparison makes up the theoretical predictions shown in Figure 5.11, where checkmarks show the set of parameters for which the TX FIFO will not fill up. The *X* symbols show those parameters that are not functional combinations.

Bandwidth can also be predicted as a fraction of the maximum available bandwidth. Theoretically, this is obtained by dividing the maximum available bandwidth 25.78 Gbps by the Core1990 bandwidth achievable with a specific transmission protocol configuration. Experimentally, bandwidth is calculated from the two accumulators on the receiving firmware by dividing the number of valid words received by the number of clock cycles.

Latency

In high-speed data transmission systems, latency is a critical performance parameter as it dictates the time it takes for data to make it from the transmitting to the receiving end, and captures the effect of all the elements that might affect timing. Theoretical modeling of latency provides a benchmark to validate measurements and performance. In this case, firmware and hardware latency are both contributors. The total latency from transmitting to receiving FPGA can comprise several contributions, all shown in Figure 5.10. The Core1990 latency values shown are estimated below:

1. Burst framing: 3 clock cycles
2. Meta framing: 7 clock cycles
3. Scrambler: 2 clock cycles
4. Encoder: 4 clock cycles
5. TX Gearbox: 67b-to-64b backpressure: 1 clock cycle

For a total of 17×2.5 ns $= 42.5$ ns.

The trigger signal output latency is estimated by num_reg$\times$clk $+$ TCO where num_reg is the total number of registers after the FIFO output register and the pin, clk is the period of one clock cycle ($\sim$0.025 ns), and TCO is the Transmission Control Protocol time. So, for the Agilex Evaluation kit, this is calculated as a range from 9.681 ns to 12.381 ns (min/max values from datasheet)

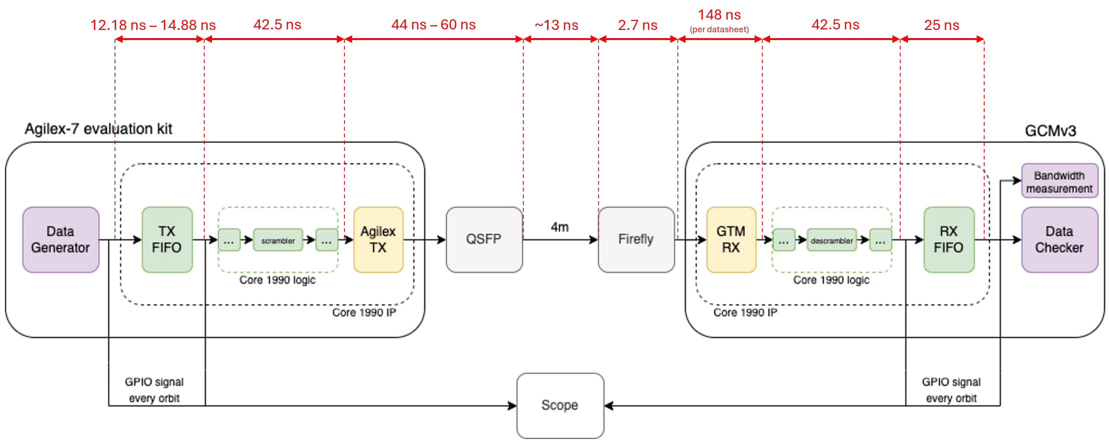

Figure 5.10: Schematic diagram of firmware logic with latency estimation values for different firmware and hardware elements.

+ 1 clk = 12.18 − 14.88 ns. For the GCM, the maximum TCO is 12.3 ns, then, the latency is: $5 \times \text{clk} + 12.5$ ns $= 25$ ns with 5 registers. Finally, the remaining values in Figure 5.10 come from: the time it takes light to travel through 4 m of optical fibre is 13 ns, and other datasheet specifications for the FireFly and GTM on the receiving firmware. Putting all these values together, the total expected latency value is in the range of 313-329 ns.

5.7 Results

5.7.1 Bandwidth Measurements

The state of the TX FIFO, i.e whether it overflowed or not, was monitored for different combinations of generated data rate and burst length. Results are shown in Figure 5.11, where observations and theoretical predictions match perfectly. These results define a region of potential working parameters in green while excluding disfavored combinations shown in red.

Furthermore, among working combinations, the received data bandwidth is at most 90 % of the maximum theoretically available bandwidth. Not only does this meet and exceed requirements discussed in [32], it is also consistent with theoretical predictions within 10 %. Figure 5.12 shows both the theoretical and measured bandwidth percentages.

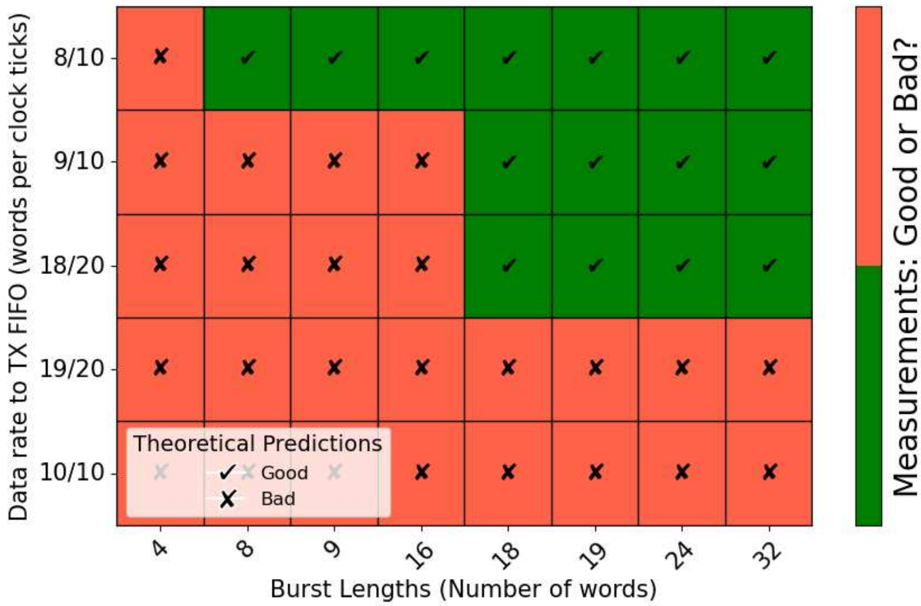

Figure 5.11: Comparison of predicted and observed state of TX FIFO for different combinations of data transmission parameters. The labels "Good" and "Bad" refer to the state of the TX FIFO; e.g whether it fills up ("Bad") or not ("Good") during data transmission. Checkmarks and x's show the theoretical predictions. Green and red shaded squares are the observed behaviour of the TX FIFO. The red region corresponds to data transmission parameters that are not operationally viable and are not considered in subsequent data transmission tests.

5.7.2 Latency Measurements

The latency measurement of interest is the time data takes from transmission to reception. Latency is measured on an oscilloscope, as shown in Figure 5.13, by using the GPIO signals sent by the firmware, and by subtracting the expected propagation time to arrive at the scope. The data transmission latency is measured consistently at around 300 ns within measurement uncertainties, as shown in Figure 5.14, demonstrating good agreement with the predicted range of 313-329 ns discussed before. The primary source of uncertainty arises from the manual placement of measurement cursors on the oscilloscope. Given the time scale used and the cursor granularity, the measurement uncertainty is roughly estimated to be ± 10 ns. This reflects the precision limits inherent to visually estimating the transition points on the waveform displayed on the oscilloscope.

Furthermore, other latencies are also measured. The latency between the start (IN) and end (OUT) of the TX and RX FIFOs was measured at 15 ns and 20 ns, respectively. These values

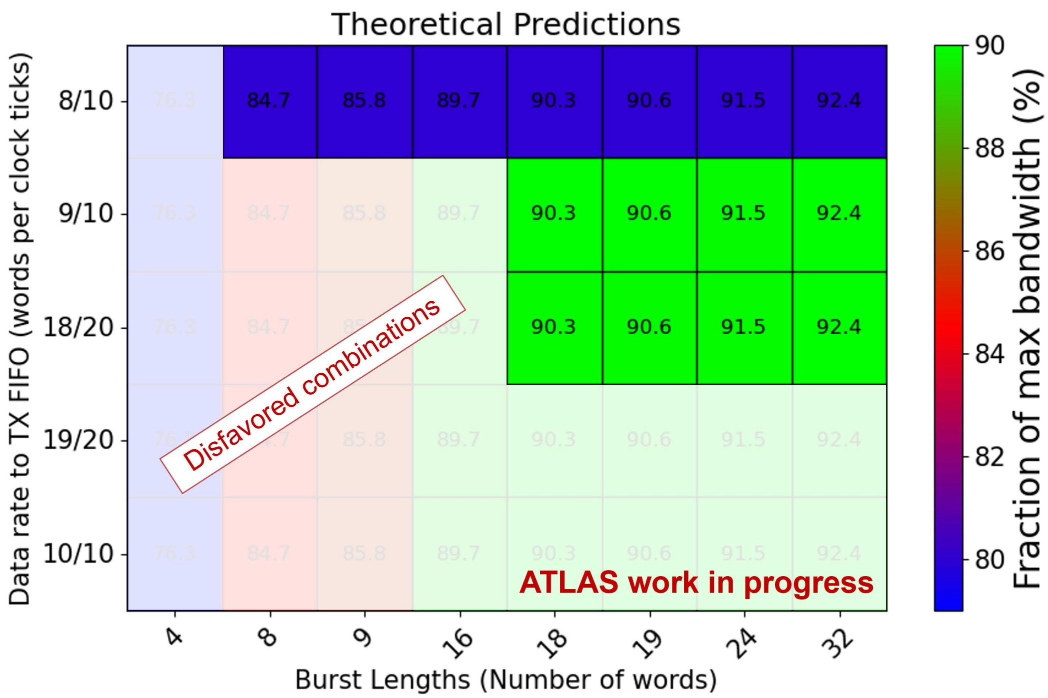

(a)

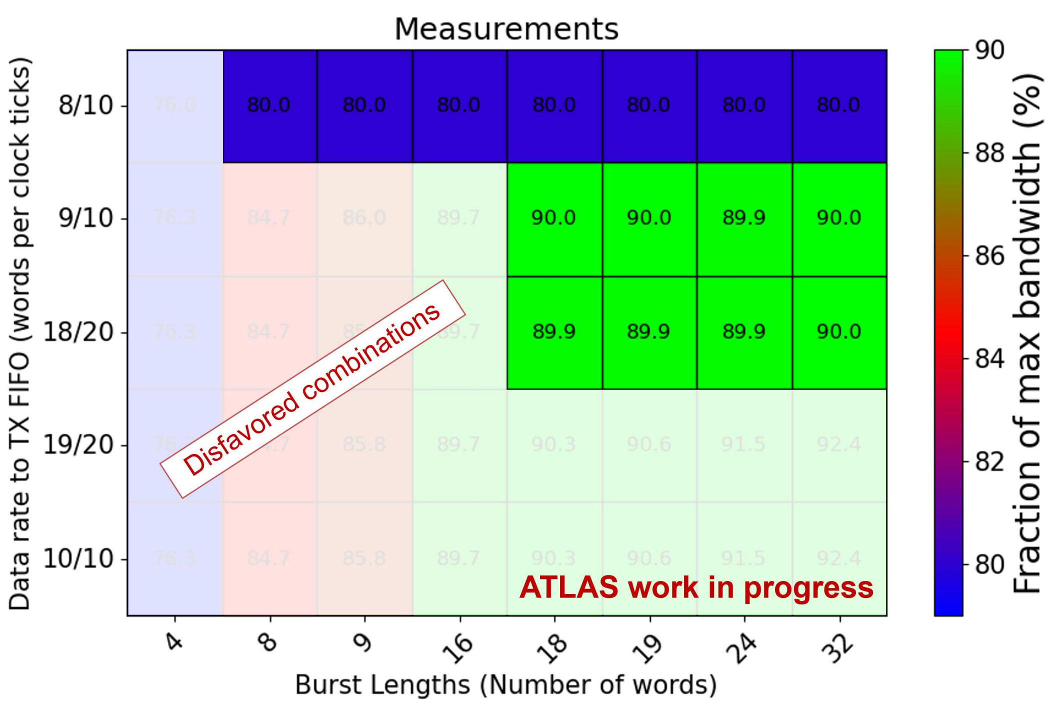

(b)

Figure 5.12: (a) Theoretical prediction of achievable bandwidth expressed as a percentage of the theoretical maximum bandwidth. (b) Measured bandwidth as a fraction of the theoretical maximum bandwidth. Only values in the upper right corner region are considered functionally viable, as those in the shaded region are disfavored combinations that lead to TX FIFO overflowing.

are in agreement with the theoretical expectations based on the firmware implementation of these FIFOs. Overall, all latency values are consistent with predicted estimates within measurement uncertainties.

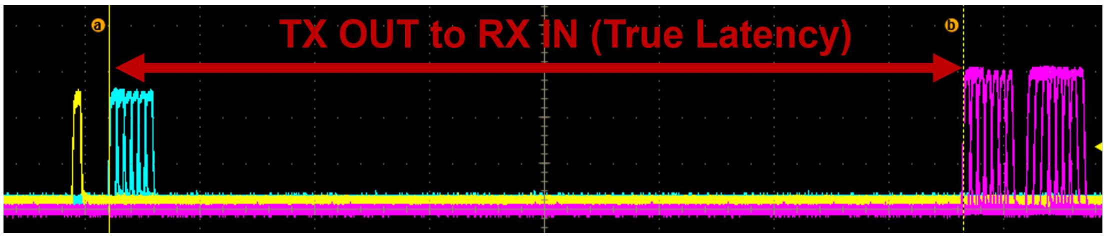

Figure 5.13: Oscilloscope screenshot of latency measurement with TX and RX flags. The yellow signal is the TX IN flag before the Core1990 logic. The blue signal is the TX out flag after the Core1990 logic.

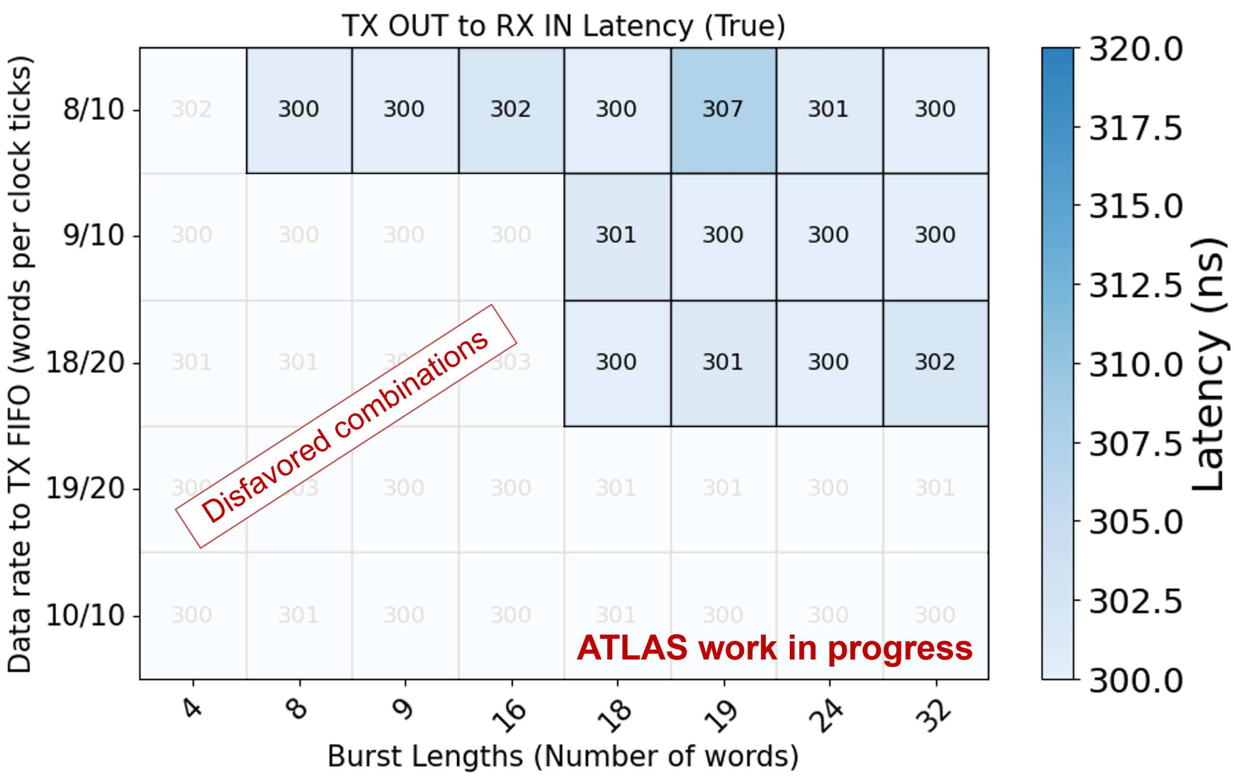

Figure 5.14: Latency measurements between TX OUT and RX IN for different generated data rates and burst lengths.

5.7.3 Attenuation Measurements

To evaluate the robustness of the optical link under varying signal conditions, attenuation measurements were conducted using an optical attenuator with gradual dB steps. The optical power was reduced in discrete steps, and the system was monitored for bit errors using the data checker on the receiving firmware. A distinct threshold is observed at 6 dB, beyond which bit errors become prominent and dominate the data stream. This procedure establishes the maximum acceptable optical power loss allowed for reliable data transmission and defines the operational margin for signal integrity.

5.7.4 Bit Error Rates

Extended data transmission stability and quality were evaluated through continuous overnight runs under nominal operating conditions. During these tests, the system presented before transmitted PRBS31-type data while the receiver continuously monitored for bit errors. No bit errors were detected throughout the duration of the overnight runs, indicating a good level of reliability and signal integrity over several hours.

5.8 Outlook

The successful test of high-speed data transfer using the Core1990 protocol and modern FPGA platforms confirms the feasibility of the upgraded LAr readout system. Data rates and latency metrics align closely with theoretical models, offering a robust solution for HL-LHC conditions. These results inform future design decisions and deployment strategies in the ATLAS detector upgrade program.

Chapter 6

Summary

This thesis presented two complementary studies that together advance both the physics program and detector capabilities of the ATLAS experiment at the Large Hadron Collider. The first part of this work focused on the data analysis of anomalous quartic gauge couplings in the $pp \to W\gamma\gamma$ process, while the second part studied data transfer between two prototype devices for the proposed high-speed readout architecture for the ATLAS Liquid Argon calorimeter electronics upgrades.

In the $W\gamma\gamma$ study, an Effective Field Theory (EFT) framework was adopted to parametrize potential deviations from the Standard Model. This enabled a systematic exploration of higher dimension operators that give rise to the quartic vertex of interest. Signal and control regions were carefully studied and re-binned differentially based on the analysis in [23] to construct a profile-likelihood model. A likelihood scan was conducted. The scans explored the parameter space of coupling coefficients that parametrize the coupling strength between the SM and new physics. The resulting scans yielded competitive constraints on the Wilson coefficients associated with the most sensitive T-type operators of the $W\gamma\gamma$ analysis. These were found to be $-1.3\ \text{TeV}^{-4} < \frac{f_{T,5}}{\Lambda^4} < 1.3\ \text{TeV}^{-4}$ and $-1.7\ \text{TeV}^{-4} < \frac{f_{T,6}}{\Lambda^4} < 1.6\ \text{TeV}^{-4}$. Additionally, 2D profile likelihood scans show correlations between the two operators and provide confidence intervals consistent with those found with the 1D scan. Interference effects can be further exploited to set even more stringent limits on the operators. These results demonstrate that the $W\gamma\gamma$ final state provides a stringent probe for the electroweak gauge structure and the study of physics beyond the Standard Model. Further work is ongoing to extend this analysis. One-dimensional and two-dimensional parameter scans will be performed to set confidence intervals on all relevant dimension-8 operators, including type-M and type-T operators. In addition, this analysis will be included in a broader ATLAS-wide study of anomalous quartic gauge couplings, which studies multiple final states. Finally, more data is being collected, which will allow for even tighter constraints through further investigation of the $W\gamma\gamma$ process.

In parallel, this thesis also addressed a key technological challenge for the future LAr calorimeter electronics upgrade: achieving robust, high-bandwidth and low-latency data transfer from the Liquid Argon Signal Processor to the Global Event Trigger Processor. For this purpose, a complete hardware and firmware setup was implemented and tested in December 2024. The implemented firmware included a customized Core1990 logic with user-configurable data rate and burst lengths to have complete control over the data payload. Transmission bandwidth and data integrity were verified across a range of parameter configurations. The tests showed successful data transmission at $\leq 90\%$ the maximum available bandwidth (25.78 Gbps) and data transfer latencies averaging at 300 ns. The latter were both in agreement with theoretical predictions. The resulting system met the stringent requirements for detector readout in the HL-LHC conditions, providing a firm basis for the next generation of ATLAS LAr calorimeter readout electronics. This work informs the future firmware and hardware design of the constituents of the new LAr electronics readout. The data tests conducted for this thesis establish a foundation for future data transfer evaluations, as both hardware and firmware continue to evolve. Once the LASP prototype boards are produced and available, similar tests to those outlined in this thesis will be repeated to validate and refine system performance.

The two studies presented in this thesis are tightly interconnected. Sensitivity to rare processes like $W\gamma\gamma$, characterized by two final-state photons measured in the LAr calorimeter, directly depends on the quality of the EM calorimeter. Advances in electronics and readout designs, especially for the proposed HL-LHC upgrade, translate into improved experimental reach for rare event topologies. So, such upgrades will allow ATLAS to pursue its physics goals at even higher luminosities, where new physics will potentially be more accessible.

By presenting both a refined analytical strategy for constraining quartic gauge interactions and a successful data transfer demonstration, this thesis supports the goal of exploiting the full discovery potential of the ATLAS experiment in the High-Luminosity LHC era.

Appendix A

Simulation of the effects of Dimension-8 Operators

This appendix summarizes the technical tricks used to implement an Effective Field Theory framework with the tools that are readily available from the first $W\gamma\gamma$ observation analysis discussed in [23]. These tools include ROOT histograms from Monte Carlo Simulations.

First, it is necessary to treat the Lagrangian in Equation 2.6 as amplitude terms. The extended SM Lagrangian can be decomposed into two types of EFT samples: namely the linear and quadratic contributions. The linear contribution, also called the interference term, represents the interaction between the SM and the EFT; it scales linearly with the coupling parameter f_j/Λ^4. The quadratic term is also known as the pure EFT term, as it only includes EFT amplitudes and scales quadratically with the coupling parameter. Finally, a novel addition to this technique is the use of cross terms, which encompass the interaction between amplitudes from different dimension-8 operators.

Decomposed samples can be combined with the Standard Model and aQGC contributions as follows:

$$|\mathcal{A}_{sm} + \sum_i c_i \mathcal{A}_i|^2 = |\mathcal{A}_{SM}|^2 + \sum_i c_i 2Re(\mathcal{A}^*_{SM}\mathcal{A}_i) + \sum_i c_i^2 |\mathcal{A}_i|^2 + \sum_{i,j,j\neq i} c_i c_j 2Re(A_i^* A_j) \quad \text{(A.1)}$$

where A_{SM} is the Standard Model amplitude, extended by adding some EFT contribution A_i with

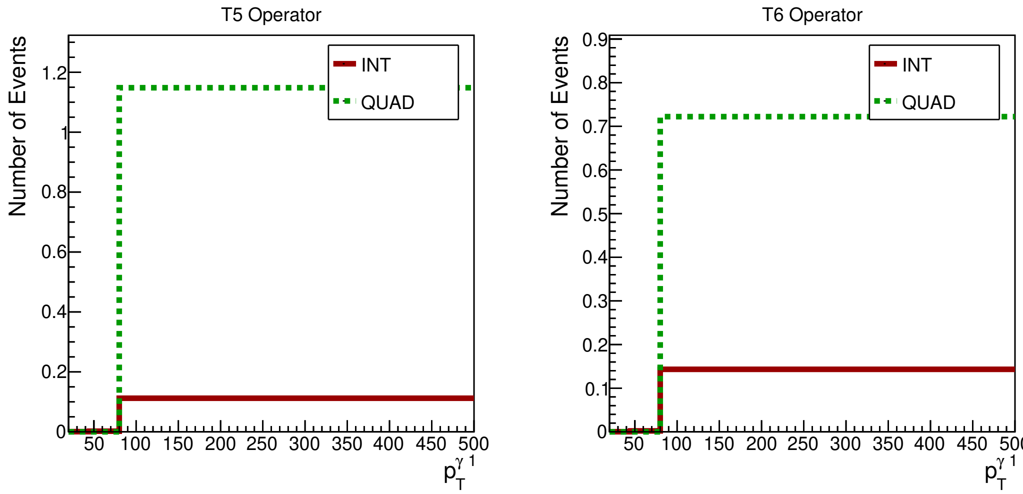

Figure A.1: Number of events predicted to come from the interference (INT) term between the SM and EFT operators, and the purely aQGC contributions (QUAD). The EFT contributions are generated and plotted with an arbitrary coupling value of $\frac{f_j}{\Lambda^4} = 1$ TeV^{-4}.

some coupling parameter c_i. This is expanded into the SM-only contribution, the interference between SM and EFT referred to as the linear term $A^*_{SM}A_i$, the aQGC-only contribution referred to as the quadratic term, and the cross term between different EFT operators A_i and A_j. Parameters c_i are fitting parameters representing the strength of the EFT contribution in the model. They typically rescale the Wilson coefficients of EFT operators, given by $c_i \propto \frac{f_j}{\Lambda^4}$, where f_j is the dimensionless Wilson coefficient, and Λ is the cutoff energy scale.

The expansion in Equation A.1 can be used to understand how EFT operators affect observables like cross-sections. This expansion directly connects to the cross-section by:

$$\sigma = \int d\Phi |\mathcal{A}|^2 \tag{A.2}$$

where σ is the total cross-section calculated by integrating over the available phase space $d\Phi$ of the squared matrix element $|\mathcal{A}|^2$. The matrix element represents the probability amplitude of a process.

Following the sensitivity conclusions gathered from Figure 4.4, it is important to understand the shape and behaviour of the EFT distributions. Figure A.1 illustrates the scaling of the linear and quadratic contributions for the two most sensitive T-type operators reweighted to a coupling value of 1 TeV^{-4}. These plots, in addition to Figure 4.4, highlight some key features. In the low to intermediate $p_T^{\gamma 1}$ region, deviations from the SM are small, and linear interference terms dominate. However, at higher values of $p_T^{\gamma 1}$, the quadratic terms dominate. Understanding the EFT scaling regime is useful to understand the dependence of the likelihood ratio test statistics to the coupling parameters of the EFT model.

List of Abbreviations

ADC	Analog to Digital Converter
ATCA	Advanced Telecommunications Computing Architecture
ATLAS	Formerly A Toroidal LHC ApparatuS (no longer an accronym)
aQGC	Anomalous Quartic gauge couplings
BSM	Beyond the Standard Model
CKM	Cabibbo-Kobayashi-Maskawa
CI	Confidence Interval
CERN	Center for European Nuclear Research
CMS	Compact Muon Solenoid
CR	Control Region
DAQ	Data AcQuisition
EFT	Effective Field Theory
EM	Electromagnetic
FEB	Front End Board
FHT	High speed Transceive
FGT	General Purpose Transceiver
FIFO	First-In First-Out
FPGA	Field Programmable Gate Array
GCM	Global Common Module
gCTPi	Global-to-CTP Interface

GEP	Global Event Processor
GbE	Gigabit Ethernet
GETP	Global Event Trigger Processor
GPIO	Geneal Purpose Input/Output
HL-LHC	High Luminosity Large Hadron Collider
JTAG	Joint Test Action Group
LAr	Liquid Argon
LASP	Liquid Argon Signal Processor
LHC	Large Hadron Collider
MUX	data Aggregators and Multiplexer
PCB	Printed Circuit Board
QGC	Quartic gauge couplings
QSFP	Quad Small Form-factor Pluggable
RF	Radio Frequency
SEOP	Start/End Of Package
SMA	SubMiniature version-A
SM	Standard Model
SMEFT	Standard Model Effective Field Theory
SoC	System on Chip
SR	Signal Region
TCO	Transmission Control Protocol
TGC	Triple gauge couplings
USB	Universal Serial Bus

List of Figures

List of Tables

Bibliography

[1] B. R. Martin and G. Shaw, *Nuclear and Particle Physics: An Introduction*. John Wiley & Sons, Ltd., 2019.

[2] S. Navas *et al.*, “Review of particle physics,” *Phys. Rev. D*, vol. 110, no. 3, p. 030001, 2024.

[3] C. Burgess and G. Moore, *The Standard Model: A Primer*. Cambridge University Press, 2006.

[4] D. Griffiths, *Introduction to Elementary Particles*. John Wiley & Sons, 1987.

[5] M. Hindmarsh, “PHYS 528 Lecture 4: Non-Abelian Gauge Theories,” 2019, Lecture notes, TRIUMF, PHYS 528.

[6] O. J. P. Éboli, and M. C. Gonzalez–Garcia, “Classifying the bosonic quartic couplings,” *Physical Review D*, vol. 93, no. 9, may 2016.

[7] S. Norbert, “The Discovery of Neutrino Masses,” in *Correlations and Fluctuations in QCD*. World Scientific, Sep. 2003, p. 5–20.

[8] R. Ahmad *et al.*, “Measurement of the Rate of nue + d –> p + p + e Interactions Produced by 8B Solar Neutrinos at the Sudbury Neutrino Observatory,” *Physical Review Letters*, vol. 87, p. , 07 2001.

[9] C. Wetterich, “Fine-tuning problem and the renormalization group,” *Physics Letters B*, vol. 140, no. 3, pp. 215–222, 1984.

[10] C. Grojean, “TASI Lectures on the Electroweak Symmetry Breaking and the Higgs Boson,” *arXiv preprint arXiv:1610.07572*, 2016.

[11] O. J. P. Eboli and M. C. Gonzalez-Garcia, “Mapping the genuine bosonic quartic couplings,” *arXiv preprint arXiv:1604.03555*, 2016.

[12] L. R. Evans and P. Bryant, “LHC Machine,” *JINST*, vol. 3, p. S08001, 2008.

[13] European Organization for Nuclear Research (CERN), “The Accelerator Complex,” Web page, 2025.

[14] E. Lopienska, “The CERN accelerator complex, layout in 2022 [Illustration],” Multimedia item on CERN Document Server, record CERN-GRAPHICS-2022-001-1, Feb. 03 2022.

[15] ATLAS Collaboration, “The ATLAS experiment at the CERN Large Hadron Collider: a description of the detector configuration for Run 3,” *JINST*, vol. 19, no. 05, p. P05063, May 2024.

[16] ATLAS Collaboration, “The ATLAS Experiment at the CERN Large Hadron Collider,” *JINST*, vol. 3, no. 08, p. S08003, aug 2008.

[17] R. M. Bianchi and ATLAS Collaboration, “ATLAS experiment schematic or layout illustration,” 2022.

[18] F. Hubaut, “Performance of the ATLAS electromagnetic calorimeter under beam tests,” *Nuclear Instruments and Methods in Physics Research Section A: Accelerators, Spectrometers, Detectors and Associated Equipment*, vol. 518, no. 1, pp. 31–35, 2004.

[19] N. Nikiforou, “Performance of the ATLAS Liquid Argon Calorimeter after three years of LHC operation and plans for a future upgrade,” 2013.

[20] ATLAS Collaboration, “ATLAS Liquid Argon Calorimeter Phase-II Upgrade: Technical Design Report,” CERN, Geneva, Tech. Rep., 2017.

[21] J. Pequenao, "Computer generated image of the ATLAS Liquid Argon," 2008.

[22] J. Pequenao and P. Schaffner, "How ATLAS detects particles: diagram of particle paths in the detector," 2013.

[23] ATLAS Collaboration, "Observation of W$\gamma\gamma$ triboson production in proton-proton collisions at s=$\sqrt{13}$ TeV with the ATLAS detector," *Physics Letters B*, vol. 848, p. 138400, 2024.

[24] ATLAS Collaboration, "Standard Model Summary Plots June 2024," CERN, Geneva, Tech. Rep., 2024.

[25] ATLAS Collaboration, "Generation request: ATLMCPROD-10184," 2025.

[26] O. Behnke, K. Kröninger, G. Schott, and T. Schörner-Sadenius, *Data analysis in high energy physics: a practical guide to statistical methods*. Weinheim: Wiley-VCH, 2013.

[27] S. S., Wilks, "The Large-Sample Distribution of the Likelihood Ratio for Testing Composite Hypotheses," *The Annals of Mathematical Statistics*, vol. 9, no. 1, pp. 60–62, 1938.

[28] EFT Tools Collaboration, "EFT-Fun: A Python framework for EFT computations," Version-controlled repository, 2025, Available at https://gitlab.cern.ch/eft-tools/eft-fun.

[29] CMS Collaboration, "CMS Public Results on Higgs Boson," 2025, Available at https://twiki.cern.ch/twiki/bin/view/CMSPublic/PhysicsResultsHIG.

[30] O. Brüning *et al.*, "The scientific potential and technological challenges of the High-Luminosity Large Hadron Collider program," *Reports on Progress in Physics*, vol. 85, no. 4, p. 046201, mar 2022.

[31] European Organization for Nuclear Research (CERN), "High Luminosity Large Hadron Collider (HL-LHC) Project," Web page, 2025.

[32] ATLAS Collaboration, "Technical Design Report for the Phase-II Upgrade of the ATLAS Trigger and Data Acquisition System - Event Filter Tracking Amendment," CERN, Geneva, Tech. Rep., 2022.

[33] Global Trigger Community, "ATLAS TDAQ Phase-II Upgrade: Hardware Specifications for the Global Trigger," Technical Report, CERN EDMS Repository, 2024, version 0.7. Retrieved from CERN EDMS (file 2677534).

[34] Intel Corporation, *Agilex™ 7 FPGA I-Series Transceiver Development Kit (6×F-Tile)*, Intel Corporation, 2025. [Online]. Available: https://www.intel.com/content/www/us/en/products/details/fpga/development-kits/agilex/si-agi040.html

[35] AMD, "Versal Adaptive SoCs and FPGAs," 2024, Product details at https://www.amd.com/en/products/adaptive-socs-and-fpgas/versal.html.

[36] EP-ESE-BE-xTCA Group, CERN, "ipmc-project: Base architecture for CERN-IPMC Software," 2018, GitLab repository, created October 03, 2018 Available at https://gitlab.cern.ch/ep-ese-be-xtca/ipmc-project .

[37] Core1990 Interlaken Contributors, "Protocol Exploration Report," OpenCores / WebSVN Repository, Technical Report Revision 5.

[38] Cortina Systems Inc. and Cisco Systems Inc., "Interlaken Protocol Definition, Revision 1.2," Interlaken Alliance, San Jose, CA, Technical Report v1.2, Oct. 7 2008.